# Electronic Supplementary Information (ESI)

## Heliconical-layered nanocylinders (HLNCs) – hierarchical self-assembly in a unique B4 phase liquid crystal morphology

Sasan Shadpour,[a] Ahlam Nemati,[a] Nicola Jane Boyd,[b] Lin Li,[c] Marianne Estelle Prévôt,[a] Samantha L. Wakerlin,[a] Julie P. Vanegas,[a] Mirosław Salamończyk,[d,e] Elda Hegmann,[a,g] Chenhui Zhu,[d] Mark R. Wilson,[b] Antal I. Jákli,[a,f] Torsten Hegmann*[a,c]

a. *Chemical Physics Interdisciplinary Program, Advanced Materials and Liquid Crystal Institute, Kent State University, Kent (Ohio) 44242-0001 USA.*

b. *Department of Chemistry, Durham University, Durham, DH1 3LE, UK*

c. *Department of Chemistry and Biochemistry, Kent State University, Kent (Ohio) 44242-0001 USA.*

d. *Advanced Light Source, Lawrence Berkeley National Laboratory, Berkeley (CA) 94720 USA.*

e. *Faculty of Chemistry, University of Warsaw, 02-089 Warszawa, Poland.*

f. *Department of Physics and Astronomy, Kent State University, Kent (Ohio) 44242-0001 USA.*

g. *Department of Biological Sciences, Kent State University, Kent (Ohio) 44242-0001 USA*

Table of Contents Page S

## 1. Materials

Commercially available chemicals and starting materials were used as purchased without further purification unless otherwise noted. All organic solvents used for synthesis were EMD Millipore-grade purified by a PureSolv solvent purification system (Innovative Technology Inc.) unless otherwise stated. Dichloromethane ($CH_2Cl_2$) and benzene ($C_6H_6$) for syntheses were dried before use with 4-Å molecular sieves overnight. Tetrahydrofuran (THF) was dried over sodium-benzophenone and distilled under a nitrogen atmosphere prior to use. All glassware used for the reactions was dried overnight at 140 °C in an oven. All reagents used were purchased from Sigma Aldrich except for 4-n-octyloxybiphenyl-4'-carboxylic acid (purchased from Synthon Chemicals GmbH & Co. KG) and for 1-ethyl-3-(3-dimethylaminopropyl)carbodiimide (EDCI) (purchased from TCI).

## 2. Methods

$^1$H NMR (400 MHz) and $^{13}$C NMR (100 MHz) spectra of the synthesized compounds were obtained using a Bruker Avance 400 MHz spectrometer in $CDCl_3$. $^1$H NMR spectra are reported in parts per million ($\delta$) relative to residual solvent peaks (7.26 ppm for $CDCl_3$ and 0.08 ppm for tetramethylsilane, TMS). $^{13}$C NMR spectra are reported in parts per million ($\delta$) relative to residual solvent peaks (77.00 for $CDCl_3$). Polarized optical microscopy (POM) observations were carried out with an Olympus BX-53 polarizing microscope equipped with a Linkam LTS420E heating/cooling stage. Phase-transition temperatures were determined using a PerkinElmer Pyris 1 differential scanning calorimeter (DSC) at a given heating and cooling rate, reporting data from the 2$^{nd}$ heating and cooling run, respectively. Thin film circular dichroism (CD) spectropolarimetry was performed using an OLIS spectrophotometer with quartz substrates. The X-ray diffraction (XRD) data were acquired using a Bruker D8 GADDS system (CuKα line, Goebel mirror, point beam collimator, Vantec2000 area detector). Samples were prepared as droplets on a heated surface controlled by Linkam-THMS-600. SAXD experiments were also carried out on beamline 7.3.3 of the Advanced Light Source of Lawrence Berkeley National Laboratory[1] (10 keV incident beam energy, 1.24 Å wavelength, utilizing a Pilatus 2 M detector). The materials were filled into 1 mm diameter quartz X-ray capillary tubes, which were then mounted into a custom-built aluminum cassette that allowed X-ray detection with ± 13.5° angular range. The cassette fits into a standard hot stage (Instec) that allowed temperature control with ± 0.1 °C precision. Analysis was done using Igor Pro software with Nika package.[2] Scanning electron microscopy (SEM) analysis was performed using a Quanta 450 FEG SEM and Nova NanoLab 200 FEG-SEM. Transmission electron microscopy (TEM) analysis was performed using JEM-1400Plus; JEOL; Peabody, MA, USA) at 90 kV. Images were taken with a 100 kV side mount camera

(Orius; GATAN; Pleasanton, CA, USA). For both electron microscopy sample preparations, the materials were dissolved in chloroform. A drop of the solution was placed on either indium tin oxide substrates for SEM or grids for TEM. After evaporation of the solvent in vacuum, the sample was heated and cooled as described for the POM experiments. Atomic force microscopy (AFM) was accomplished by a Bruker Dimension Icon microscope working in tapping mode. Cantilevers with a spring constant k ~ 0.4 N/m were used with the working resonant frequency ~70-80 kHz. Robertson Microlit Laboratories (NJ) did elemental (CHN) analysis.

## 3. Synthesis

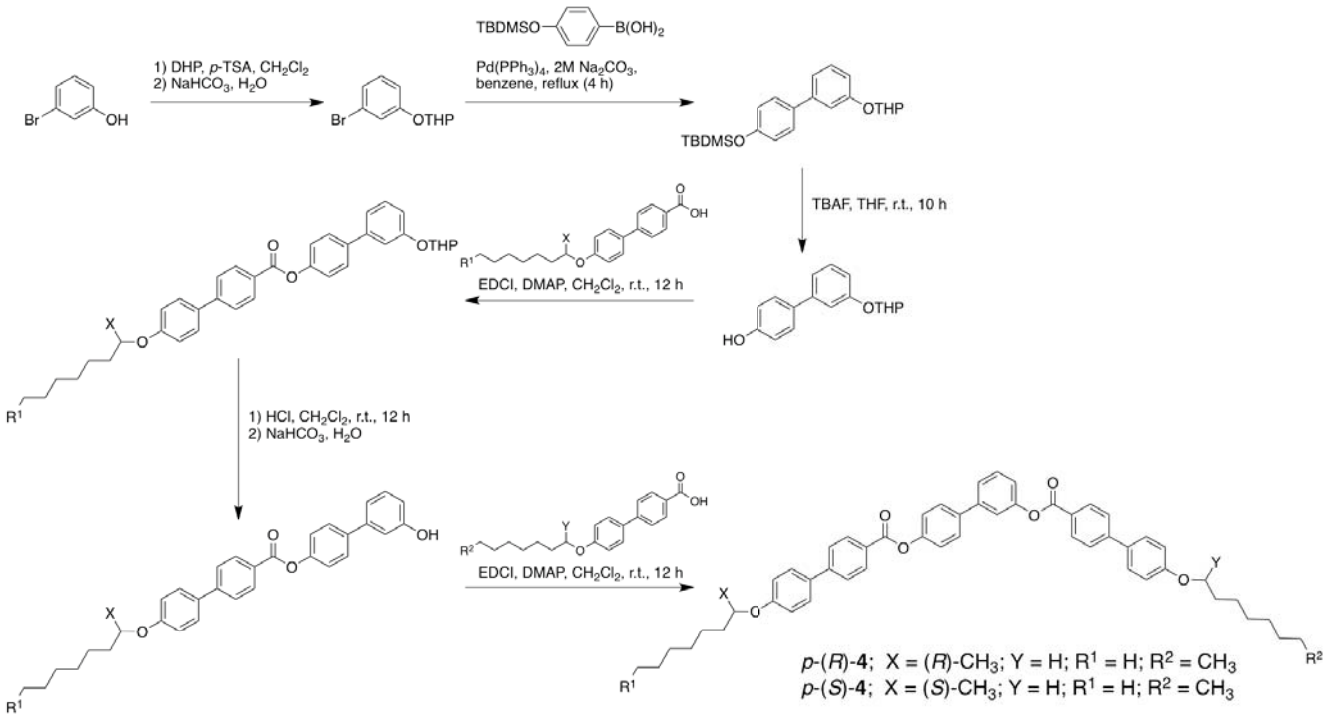


**Scheme S1.** Synthetic route pursed to obtain compounds *p*-(*R*)-**4** and *p*-(*S*)-**4**.

The synthesis of *p*-(*R*)-**4** and *p*-(*S*)-**4** was accomplished following the synthetic route outlined in Scheme S1. The synthesis of various intermediates has been reported previously.[3, 4]

### 3.1. 4'-[4-(2-(*R*)-heptan-2-yloxy)biphenyloxy]-3-tetrahydropyranyloxybiphenyl

This compound was synthesized under an inert gas atmosphere conditions, where 4'-hydroxy-3-tetrahydro-pyranyloxybiphenyl (141.4 mg, 0.52 mmol), 4'-[2-(*R*)-heptan-2-yloxy]biphenyl-4-carboxylic acid (220.2 mg, 0.68 mmol), and 4-(dimethylamino)pyridine (DMAP) (147 mg, 1.18 mmol) were combined and dissolved in a mixture of

dichloromethane (5 mL) and THF (5 mL) and stirred for 5 minutes. EDCI (301.5 mg, 1.57 mmol) was then added to the reaction mixture. The reaction was kept under stirring at room temperature under $N_2$ for 24 hours and followed by TLC. The resulting mixture was washed with saturated NaCl solution, extracted with $CHCl_3$, and then dried over anhydrous $Na_2SO_4$. The filtrate was collected by filtration and the remaining solution concentrated by rotary evaporation under reduced pressure. The residue was deposited onto silica and purified by column chromatography with $CHCl_3$ as eluent to yield a white solid (202.9 mg, 67.5%).

$^1$H NMR ($CDCl_3$, 400 MHz, *δ*/ppm): *δ* 8.28 (dt, 2H, *J* = 8.42, 1.80 Hz, biphenyl), 7.72 (dt, 2H, *J* = 8.78, 1.80 Hz, biphenyl), 7.67 (dt, 2H, *J* = 8.42, 2.93 Hz, biphenyl), 7.62 (dt, 2H, biphenyl *J* = 8.78, 2.20 Hz,), 7.37 (t, 1H, *J* = 7.68 Hz, biphenyl), 7.29-7.31 (m, 3H, biphenyl), 7.27 (dt, 1H, *J* = 7.7, 1.1 Hz, biphenyl), 7.01-7.09 (m, 1H, biphenyl), 6.99 (dt, 2 H, *J* = 8.78, 2.93 Hz, biphenyl), 5.51 (t, 1H, *J* = 3.11 Hz, -OC$\underline{H}$($CH_2$-)-O-, THP), 4.48 (t, 1H, *J* = 6.59 Hz, -OC$\underline{H}$($CH_3$)-$C_7H_{15}$), 3.93- 3.99 (m, 1H, -O-C$\underline{H_a}H_b$-$CH_2$-, THP), 3.63-3.66 (m, 1H, -O-$CH_a\underline{H_b}$-$CH_2$-, THP), 1.80-1.93 (m, 3+2H, THP, -$OC_2H_4$-C$\underline{H_2}$-$C_5H_{11}$), 1.62-1.75 (m, 3H, THP), 1.46-1.53 (m, 11H, -$OCH_2$-C$\underline{H_3}$-$C_4\underline{H_8}$), 0.90 (t, 3H, *J* = 6.95 Hz, -C$\underline{H_3}$). $^{13}$C NMR ($CDCl_3$, 100 MHz, *δ*/ppm): 158.70, 157.48, 150.47, 146.02, 141.79, 138.78, 131.81, 130.73, 129.72, 128.44, 128.24, 127.41, 126.57, 121.95, 120.47, 116.16, 115.47, 115.26, 96.43, 74.01, 62.08, 36.46, 31.79, 30.41, 29.28, 25.54, 25.22, 22.60, 19.75, 18.79, 14.08.

### 3.2. 4'-[4-(2-(*S*)-heptan-2-yloxy)biphenyloxy]-3-tetrahydropyranyloxybiphenyl

The enantiomer was synthesized in the same way. Quantities: 4'-hydroxy-3-tetrahydropyranyloxybiphenyl (141.4 mg, 0.52 mmol), 4'-[2-(*S*)-heptan-2-yloxy]biphenyl-4-carboxylic acid (220.2 mg, 0.68 mmol), (DMAP) (147 mg, 1.18 mmol), and EDCI (301.5 mg, 1.57 mmol). $^1$H NMR ($CDCl_3$, 400 MHz, *δ*/ppm): *δ* 8.28 (dt, 2H, *J* = 8.42, 1.80 Hz, biphenyl), 7.72 (dt, 2H, *J* = 8.78, 1.80 Hz, biphenyl), 7.67 (dt, 2H, *J* = 8.42, 2.93 Hz, biphenyl), 7.62 (dt, 2H, biphenyl, *J* = 8.78, 2.20 Hz,), 7.37 (t, 1H, *J* = 7.68 Hz, biphenyl), 7.29-7.31 (m, 3H, biphenyl), 7.27 (dt, 1H, *J* = 7.7, 1.1 Hz, biphenyl), 7.01-7.09 (m, 1H, biphenyl), 6.99 (dt, 2H, *J* = 8.78, 2.93 Hz, biphenyl), 5.51 (t, 1H, *J* = 3.11 Hz, -OC$\underline{H}$($CH_2$-)-O-, THP), 4.48 (t, 1H, *J* = 6.59 Hz, -OC$\underline{H}$($CH_3$)-$C_7H_{15}$), 3.93-3.99 (m, 1H, -O-C$\underline{H_a}H_b$-$CH_2$-, THP), 3.63-3.66 (m, 1H, -O-$CH_a\underline{H_b}$-$CH_2$-, THP), 1.80-1.93 (m, 3+2H, THP, -$OC_2H_4$-C$\underline{H_2}$-$C_5H_{11}$), 1.62-1.75 (m, 3H, THP), 1.46-1.53 (m, 11H, -$OCH_2$-$CH_3$-$C_4\underline{H_8}$), 0.90 (t, 3H, *J* = 6.95 Hz, -C$\underline{H_3}$). $^{13}$C NMR ($CDCl_3$, 100 MHz, *δ*/ppm): 165.23, 158.76, 157.54, 150.53, 146.05, 141.83, 138.82, 130.79, 128.49, 128.29, 126.61, 122.02, 120.51, 116.20, 96.47, 74.03, 62.11, 36.52, 31.87, 30.46, 29.34, 25.60, 25.28, 22.67, 19.80, 18.85, 14.17.

### 3.3. 4'-[4-(2-(*R*)-heptan-2-yloxy)biphenyloxy]-3-hydroxybiphenyl

In a round-bottom flask 4'-[4-(2-(*R*)-heptan-2-yloxy)biphenyloxy]-3-tetrahydropyranyloxybiphenyl (105 mg, 0.184 mmol) was dissolved in $CH_2Cl_2$ (13 mL) followed by addition of HCl (36%, 162 μL). The solution was stirred at room temperature for 18 hours and monitored throughout by TLC. To this mixture, $NaHCO_3$ (0.5 g) and water (20 mL) were added. The solid was filtered off and washed with $CHCl_3$. The organic phase was dried over anhydrous $Na_2SO_4$. The filtrate was collected by filtration and then concentrated by rotary evaporation under reduced pressure. The residue was purified by column chromatography ($CHCl_3$ / MeOH = 10 / 0.5) to yield a white solid (64 mg, 71.1%).

$^1$H NMR ($CDCl_3$, 400 MHz, *δ*/ppm): *δ* 8.26 (dt, 2H, *J* = 8.78 Hz, 1.46 Hz, biphenyl), 7.71 (dt, 2H, *J* = 8.78 HZ, 1.93 Hz, biphenyl), 7.60-7.66 (m, 4H, biphenyl), 7.30-7.33 (m, 3H, biphenyl), 7.27 (dt, 1H, *J* = 8.4 Hz, 2.2 Hz, biphenyl), 7.16-7.19 (m, 1H, biphenyl), 7.01-7.07 (m, 2H, biphenyl), 6.86 (dt, 1H, *J* = 7.78 Hz, 2.93 Hz, biphenyl), 4.87 (s, 1H, *J* = 6.97, -O$\underline{H}$) 4.40-4.48(m, 1H, *J* = 6.6 Hz, -OC$\underline{H}_2C_7H_{15}$), 1.75-1.83 (m, 1H, -CHC$\underline{H}_a$$H_b$$C_6H_{13}$), 1.60-1.67 (m, 1H, -CHC$H_a$$\underline{H}_b$$C_6H_{13}$), 1.26-1.60 (m, 3H+8H, -O(C$\underline{H}_3$)$C_3H_6$-$C_4$$\underline{H}_8$-$CH_3$), 0.90 (t, 3H, -C$\underline{H}_3$). $^{13}$C NMR ($CDCl_3$, 100 MHz, *δ*/ppm): 165.21, 158.70, 155.85, 150.55, 146.05, 142.17, 138.46, 131.79, 130.74, 140.04, 128.44, 128.18, 127.34, 126.58, 122.00, 119.75, 116.17, 114.25, 114.05, 74.03, 36.46, 31.80, 29.27, 25.53, 22.61, 19.74, 14.09.

### 3.4. 4'-[4-(2-(*S*)-heptan-2-yloxy)biphenyloxy]-3-hydroxybiphenyl

The enantiomer was synthesized in the same way as 3.3. Quantities: 4'-[4-(2-(*S*)-heptan-2-yloxy)biphenyloxy]-3-tetrahydropyranyloxybiphenyl (105 mg, 0.184 mmol), HCl (36%, 165 μL), and $NaHCO_3$ (0.5 g) in water (20 mL).

$^1$H NMR ($CDCl_3$, 400 MHz, *δ*/ppm): *δ* 8.26 (dt, 2H, *J* = 8.78 Hz, 1.46 Hz, biphenyl), 7.71 (dt, 2H, *J* = 8.78 HZ, 1.93 Hz, biphenyl), 7.60-7.66 (m, 4H, biphenyl), 7.30-7.33 (m, 3H, biphenyl), 7.27 (dt, 1H, *J* = 8.4 Hz, 2.2 Hz, biphenyl), 7.16-7.19 (m, 1H, biphenyl), 7.01-7.07 (m, 2H, biphenyl), 6.86 (dt, 1H, *J* = 7.78 Hz, 2.93 Hz, biphenyl), 4.87 (s, 1H, *J* = 6.97, -O$\underline{H}$) 4.40-4.48(m, 1H, *J* = 6.6 Hz, -OC$\underline{H}_2C_7H_{15}$), 1.75-1.83 (m, 1H, -CHC$\underline{H}_a$$H_b$$C_6H_{13}$), 1.60-1.67 (m, 1H, -CHC$H_a$$\underline{H}_b$$C_6H_{13}$), 1.26-1.60 (m, 3H+8H, -O(C$\underline{H}_3$)$C_3H_6$-$C_4$$\underline{H}_8$-$CH_3$), 0.90 (t, 3H, -C$\underline{H}_3$). $^{13}$C NMR ($CDCl_3$, 100 MHz, *δ*/ppm): 163.21, 158.40, 156.85, 150.55, 146.05, 142.17, 138.46, 131.79, 130.74, 140.04, 130.82, 128.49, 128.20, 126.64, 122.00, 119.51, 116.26, 114.25, 114.05, 74.15, 36.50, 31.85, 29.33, 25.58, 22.65, 19.79, 14.14.

### 3.5. 4'-[4-(2-(*R*)-heptan-2-yloxy)biphenyloxy]-3-[4-(4'-[4'-Octyloxy]biphenyl)]biphenyl, *p*-(*R*)-4

In a $N_2$-purged flask, 4'-[4-(2-(*R*)-heptan-2-yloxy)biphenyloxy]-3-hydroxybiphenyl (64 mg, 0.137 mmol), 4'-[4-octyloxy]biphenyl-4-carboxylic acid (53.7 mg, 0.165 mmol), and DMAP (20.8 mg, 0.170 mmol) were dissolved in a mixture of dichloromethane (5 mL) and THF (5 mL) and stirred for 5 minutes. Then, EDCI (33.2 mg, 0.173 mmol) was added. The reaction was kept under stirring at room temperature under $N_2$ for 18 hours and followed by TLC. The

resulting mixture was washed with saturated NaCl solution, extracted with $CHCl_3$, and then dried over anhydrous $Na_2SO_4$. The filtrate was collected by filtration and concentrated by rotary evaporation under reduced pressure. The residue was deposited onto silica and purified by column chromatography with $CHCl_3$ to yield a white solid (109 mg, 98.9%).

$^1$H NMR ($CDCl_3$, 400 MHz, *δ*/ppm): *δ* 8.30 (dd, 4H, *J* = 8.3, 4.9 Hz, biphenyl), 7.74 (dd, 6H, *J* = 8.5, 2.1 Hz, biphenyl), 7.64 (dd, 4H, *J* = 8.7, 3.8 Hz, biphenyl), 7.57 – 7.50 (m, 3H, biphenyl), 7.36 (d, 2H, *J* = 8.6 Hz, biphenyl), 7.29 (s, 1H, biphenyl), 7.04 (dd, 4H, *J* = 8.6, 5.9 Hz, biphenyl), 4.46 (q, 1H, *J* = 6.1 Hz, -$OCHCH_3$-), 4.05 (t, 2H, *J* = 6.6 Hz, -$OCH_2$-$C_7H_{15}$), 1.86 (s, 2H+1H, - $OCH_2CH_2C_6H_{13}$, -$OCHCH_3CH_aCH_b$), 1.62 (s, 1H, -$OCHCH_3CH_aCH_b$-), 1.52 (s, 3H), 1.43 – 1.30 (m, 18H), 0.94 (s, 3H+3H, *J* = 6.95 Hz, -$OCHCH_3CH_aH_bC_4H_8CH_3$, $OC_7H_{14}CH_3$). $^{13}$C NMR (100 MHz, $CDCl_3$): *δ* 165.17, 159.61, 158.74, 151.46, 150.77, 146.05, 142.08, 137.97, 131.96, 131.81, 130.77, 129.86, 128.46, 128.32, 127.44, 126.63, 124.62, 122.14, 120.69, 120.51, 116.20, 115.01, 77.37, 77.05, 76.73, 74.05, 68.19, 36.50, 31.86, 29.40, 29.28, 26.09, 25.57, 22.70, 19.78, 14.15. Elemental analysis - Calculated for $C_{54}H_{58}O_6$: C, 80.77; H, 7.28; Found: C, 80.52; H, 7.46.

### 3.6. 4'-[4-(2-(S)-heptan-2-yloxy)biphenyloxy]-3-[4-(4'-[4'-Octyloxy]biphenyl)]biphenyl, *p*-(*S*)-4

The enantiomer compound *p*-(*S*)-**4** was synthesized in the same way as *p*-(*R*)-**4**. Quantities: 4'-[4-(2-(*S*)-heptan-2-yloxy)biphenyloxy]-3-hydroxybiphenyl (64 mg, 0.137 mmol), 4'-[4-octyloxy]biphenyl-4-carboxylic acid (53.7 mg, 0.165 mmol), DMAP (20.8 mg, 0.170 mmol), and EDCI (33.2 mg, 0.173 mmol).

$^1$H NMR ($CDCl_3$, 400 MHz, *δ*/ppm): *δ* 8.30 (dd, 4H, *J* = 8.3, 4.9 Hz, biphenyl), 7.74 (dd, 6H, *J* = 8.5, 2.1 Hz, biphenyl), 7.64 (dd, 4H, *J* = 8.7, 3.8 Hz, biphenyl), 7.57 – 7.50 (m, 3H, biphenyl), 7.36 (d, 2H, *J* = 8.6 Hz, biphenyl), 7.29 (s, 1H, biphenyl), 7.04 (dd, 4H, *J* = 8.6, 5.9 Hz, biphenyl), 4.46 (q, 1H, *J* = 6.1 Hz, -$OCHCH_3$-), 4.05 (t, 2H, *J* = 6.6 Hz, -$OCH_2$-$C_7H_{15}$), 1.86 (s, 2H+1H, - $OCH_2CH_2C_6H_{13}$, -$OCHCH_3CH_aCH_b$), 1.62 (s, 1H, -$OCHCH_3CH_aCH_b$-), 1.52 (s, 3H), 1.43 – 1.30 (m, 18H), 0.94 (s, 3H+3H, *J* = 6.95 Hz, -$OCHCH_3CH_aH_bC_4H_8CH_3$, $OC_7H_{14}CH_3$). $^{13}$C NMR (101 MHz, CDCl3): *δ* 165.17, 159.61, 158.74, 151.46, 150.77, 146.05, 142.08, 137.97, 131.96, 131.81, 130.77, 129.86, 128.46, 128.32, 127.44, 126.63, 124.62, 122.14, 120.69, 120.51, 116.20, 115.01, 77.37, 77.05, 76.73, 74.05, 68.19, 36.50, 31.86, 29.40, 29.28, 26.09, 25.57, 22.70, 19.78, 14.15. Elemental analysis - Calculated for $C_{54}H_{58}O_6$: C, 80.77; H, 7.28. Found: C, 80.51; H, 7.21.

## 4. NMR spectra

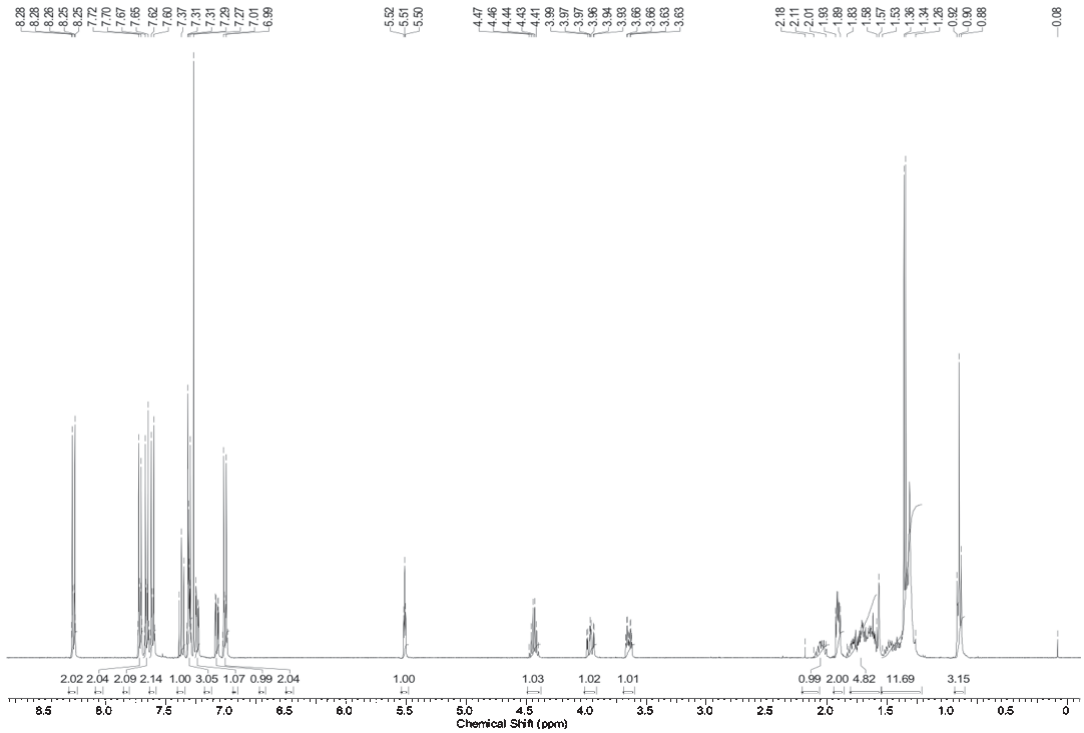


**Figure S1.** $^{1}$H NMR spectrum of compound under heading **3.1**.

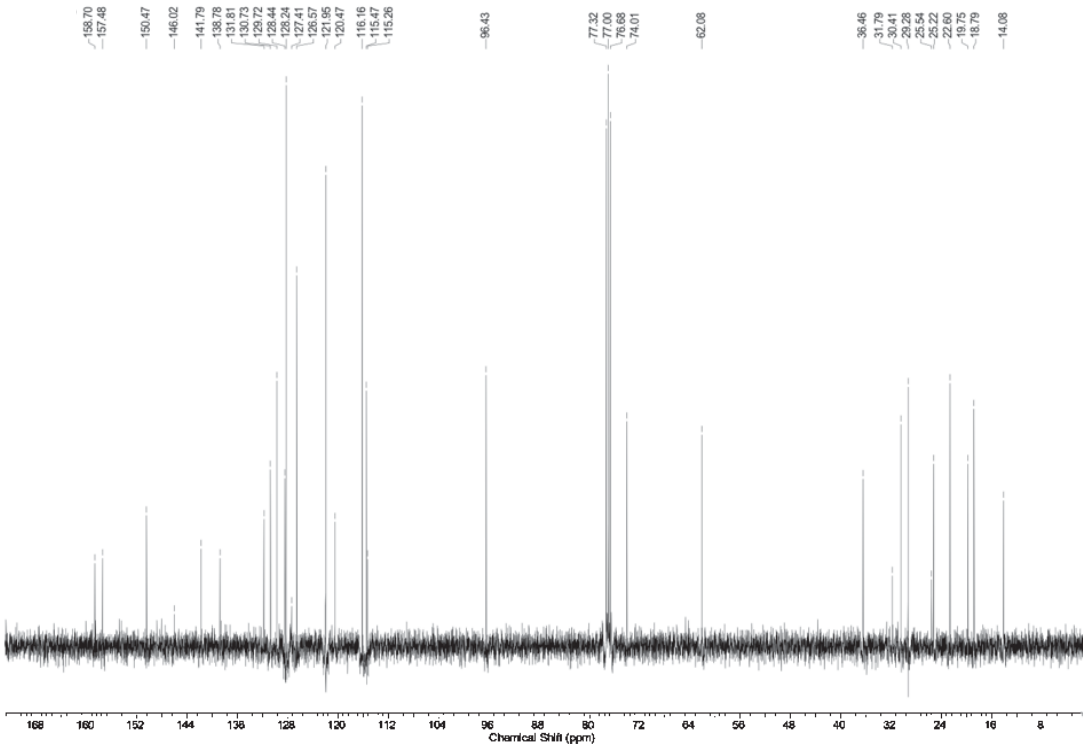


**Figure S2.** $^{13}$C NMR spectrum of compound under heading **3.1**.

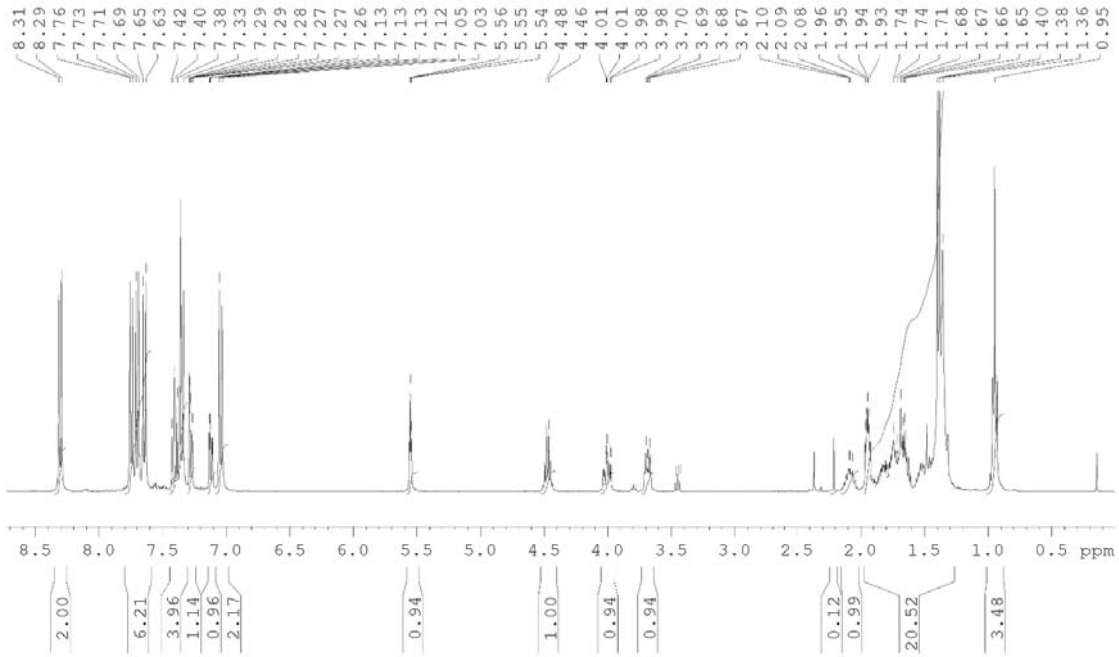


**Figure S3.** $^{1}$H NMR spectrum of compound under heading **3.2**.

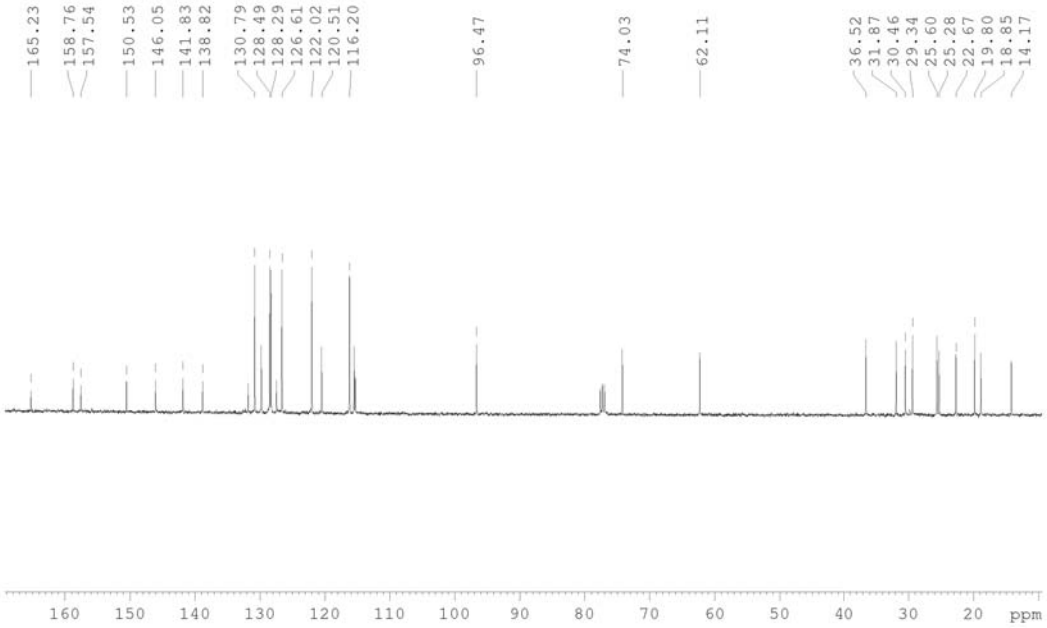


**Figure S4.** $^{13}$C NMR spectrum of compound under heading **3.2**.

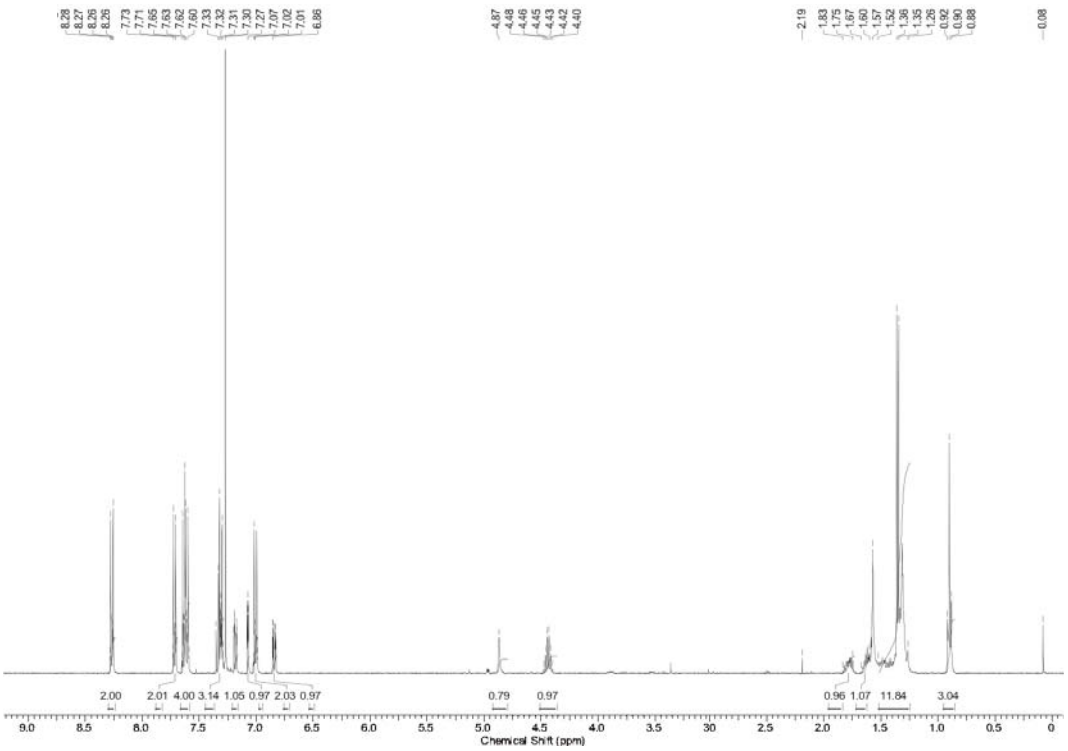


**Figure S5.** $^{1}$H NMR spectrum of compound under heading **3.3**.

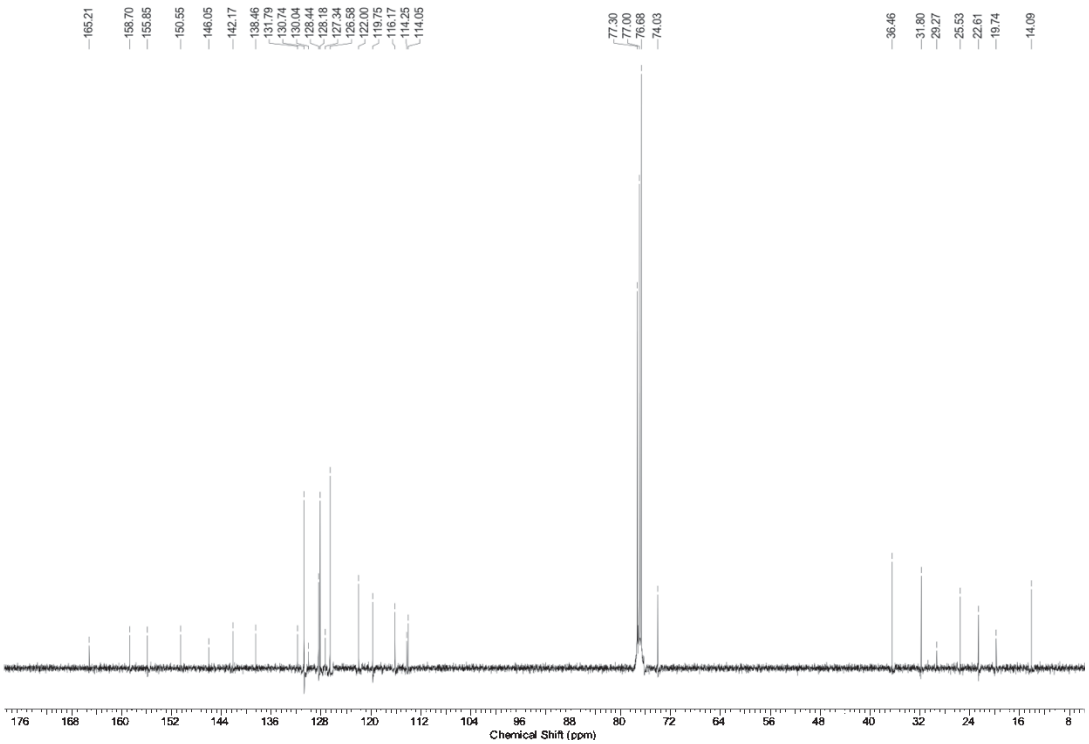


**Figure S6.** $^{13}$C NMR spectrum of compound under heading **3.3**.

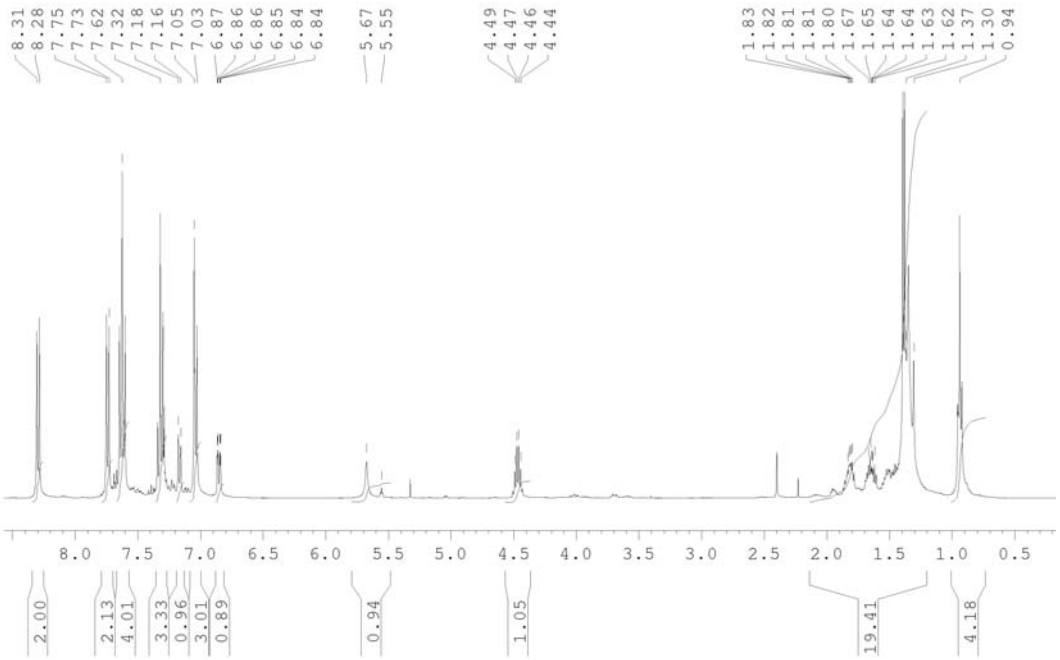


**Figure S7.** $^{1}$H NMR spectrum of compound under heading **3.4**.

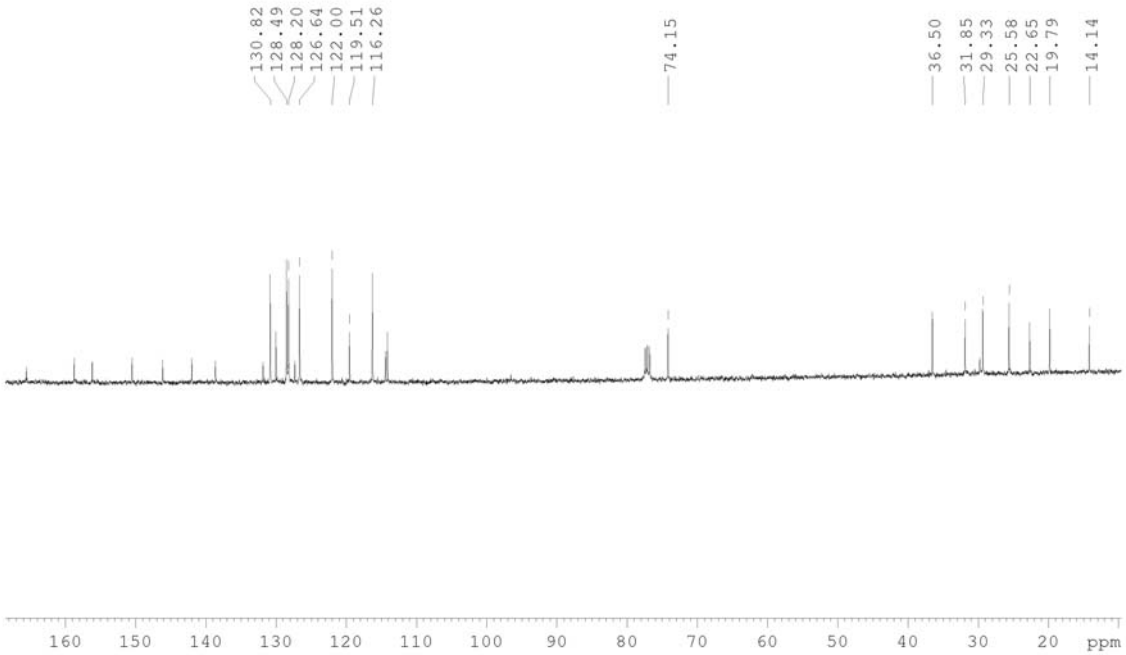


**Figure S8.** $^{13}$C NMR spectrum of compound under heading **3.4**.

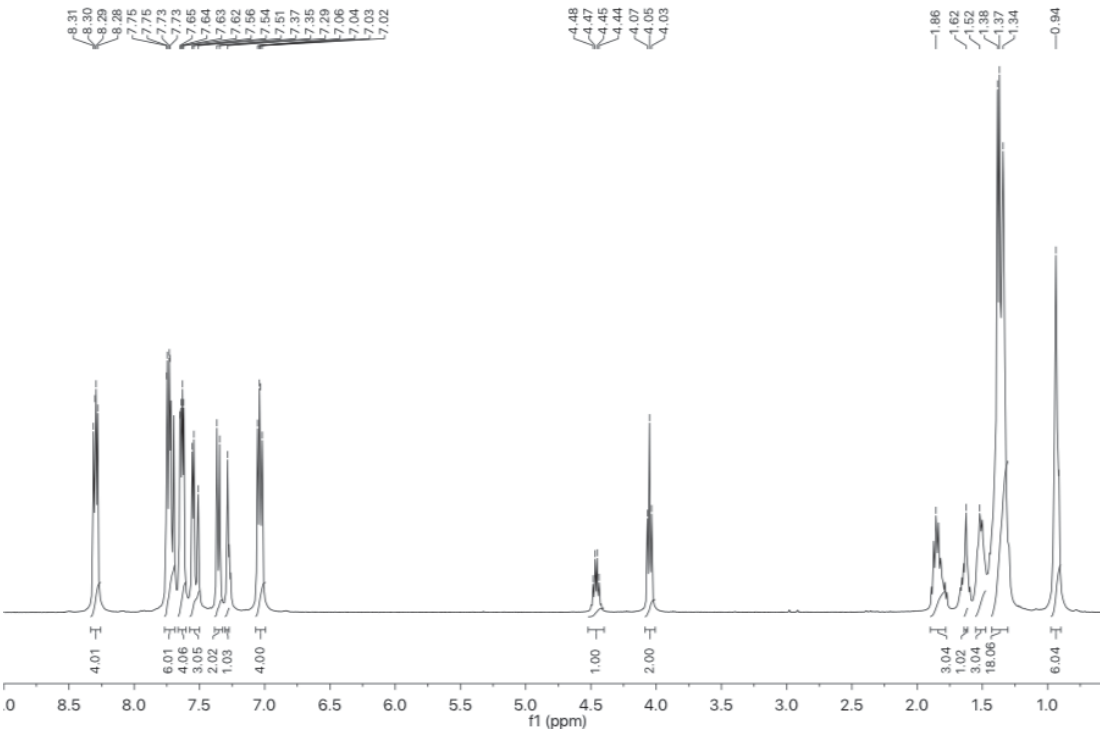


**Figure S9.** $^{1}$H NMR spectrum of *p*-(*R*)-**4**.

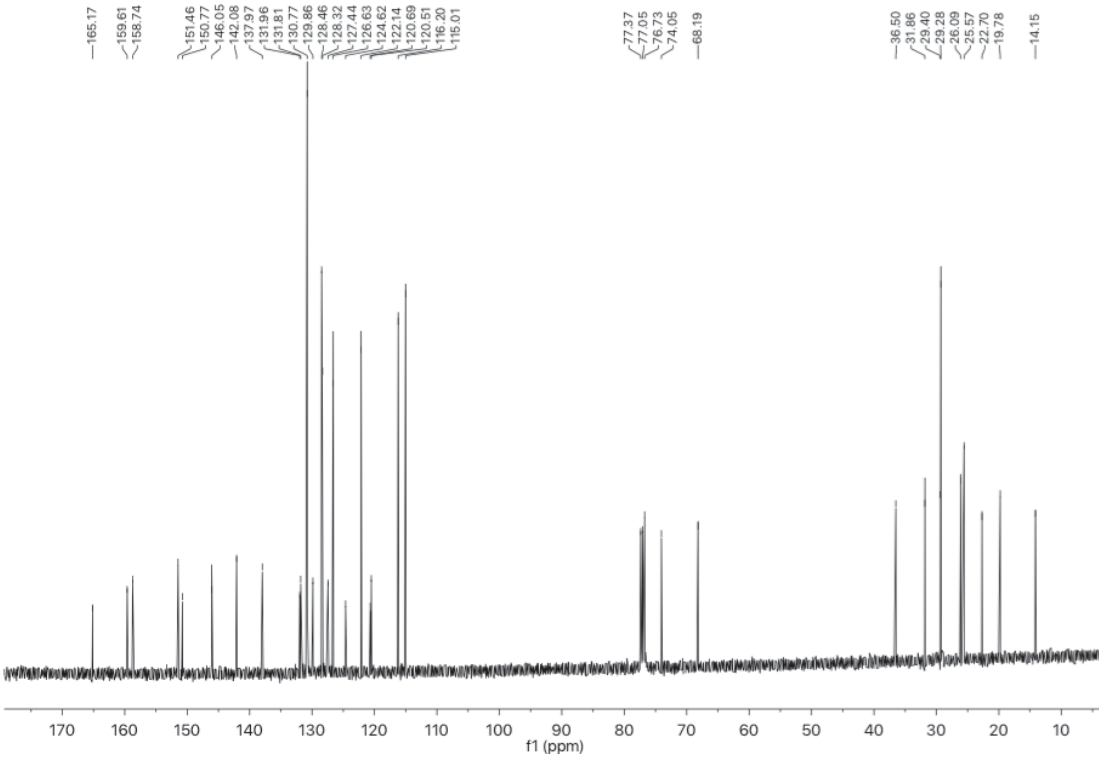


**Figure S10.** $^{13}$C NMR spectrum of *p*-(*R*)-**4**.

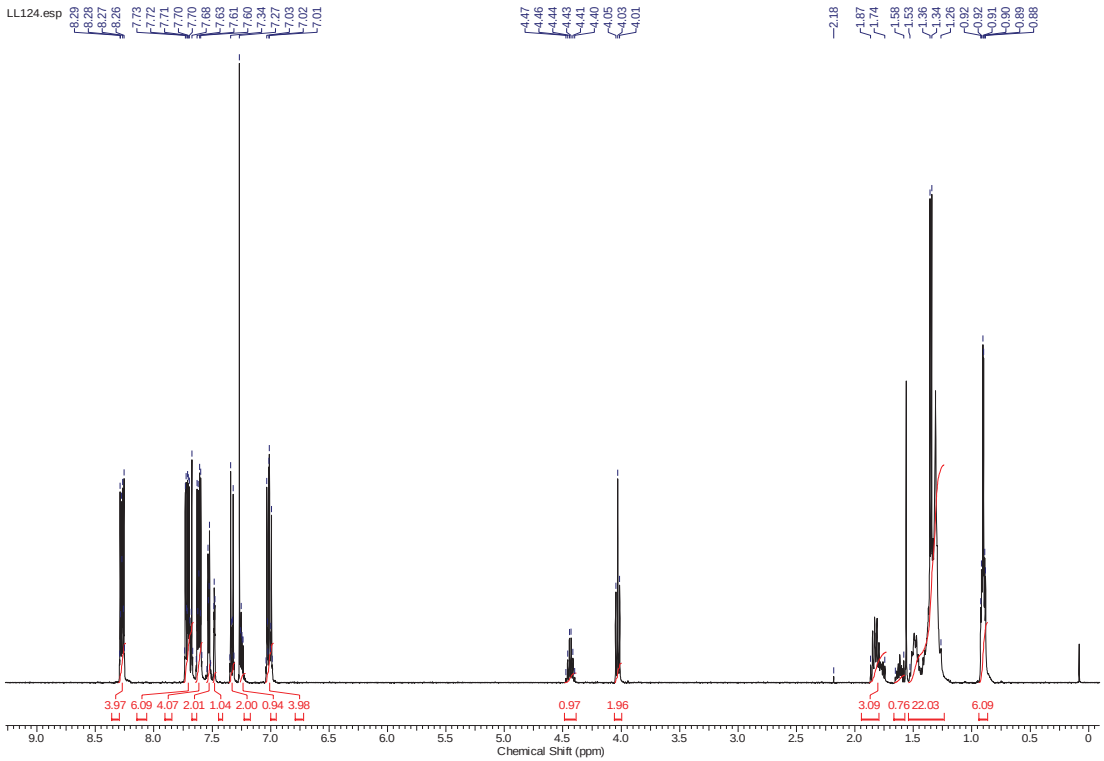


**Figure S11.** $^{1}$H NMR spectrum of *p*-(*S*)-**4**.

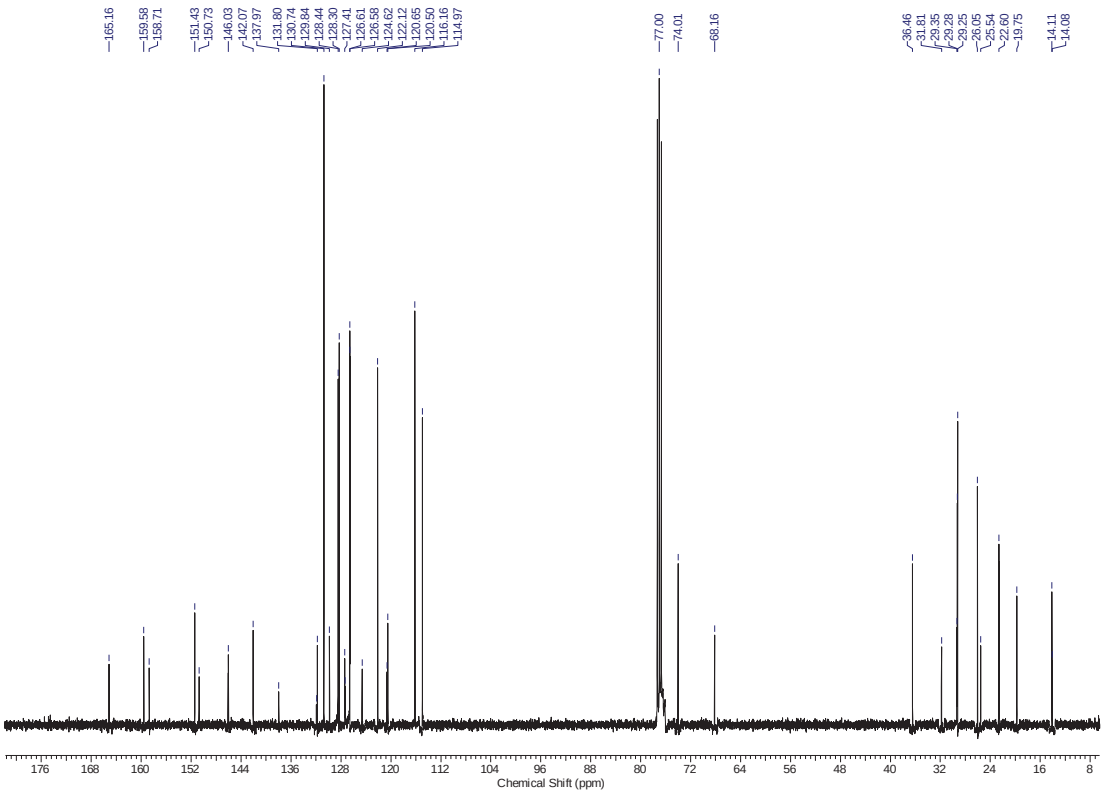


**Figure S12.** $^{13}$C NMR spectrum of *p*-(*S*)-**4**.

## 5. Additional Polarized optical microscopy images

When the B4 phase (HLNC morphology) is confined between two pre-cleaned untreated glass substrates additional self-assembly features become apparent also by POM. The nanocylinders form in a tangential fashion upon slow cooling at a rate of 5 °C $min^{-1}$. POM images show this assembly, which can be further visualized by viewing the sample using a quarter wave retarder indicating the different brightness of brushes with respect to changing the director of the nanocylinder assemblies.

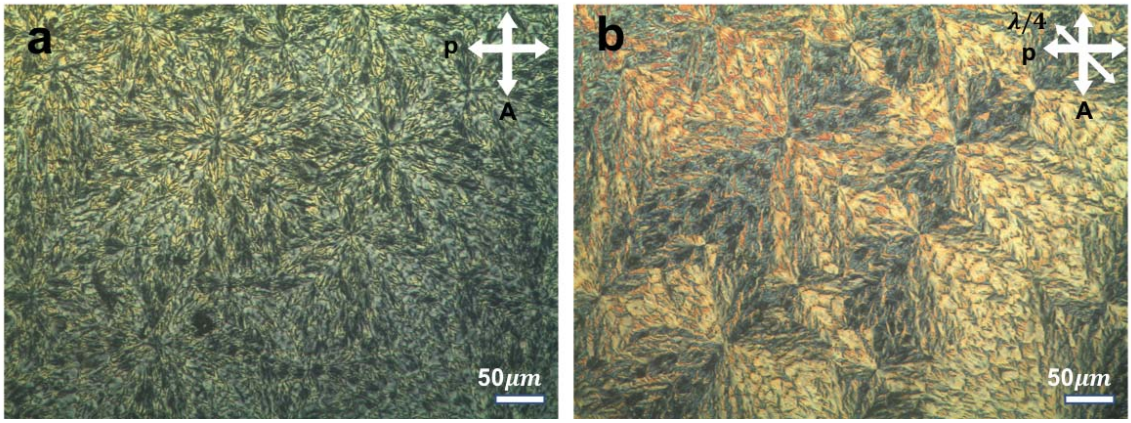


**Figure S13.** POM images of *p*-(*R*)-**4** upon slow cooling: **a** image is taken under crossed polarizer / analyser, **b** the same condition as in image **a** after inserting a quarter wave retarder that indicates the tangential assembly as in the AFM images shown in Figure S23.

**5.1** Additional polarized light optical microscopy images for *p*-(*R*)-**4** on heating and cooling at a rate of 5 °C min$^{-1}$ as well as on fast cooling (quenching sample from the isotropic liquid phase) are collected in Figure S14.

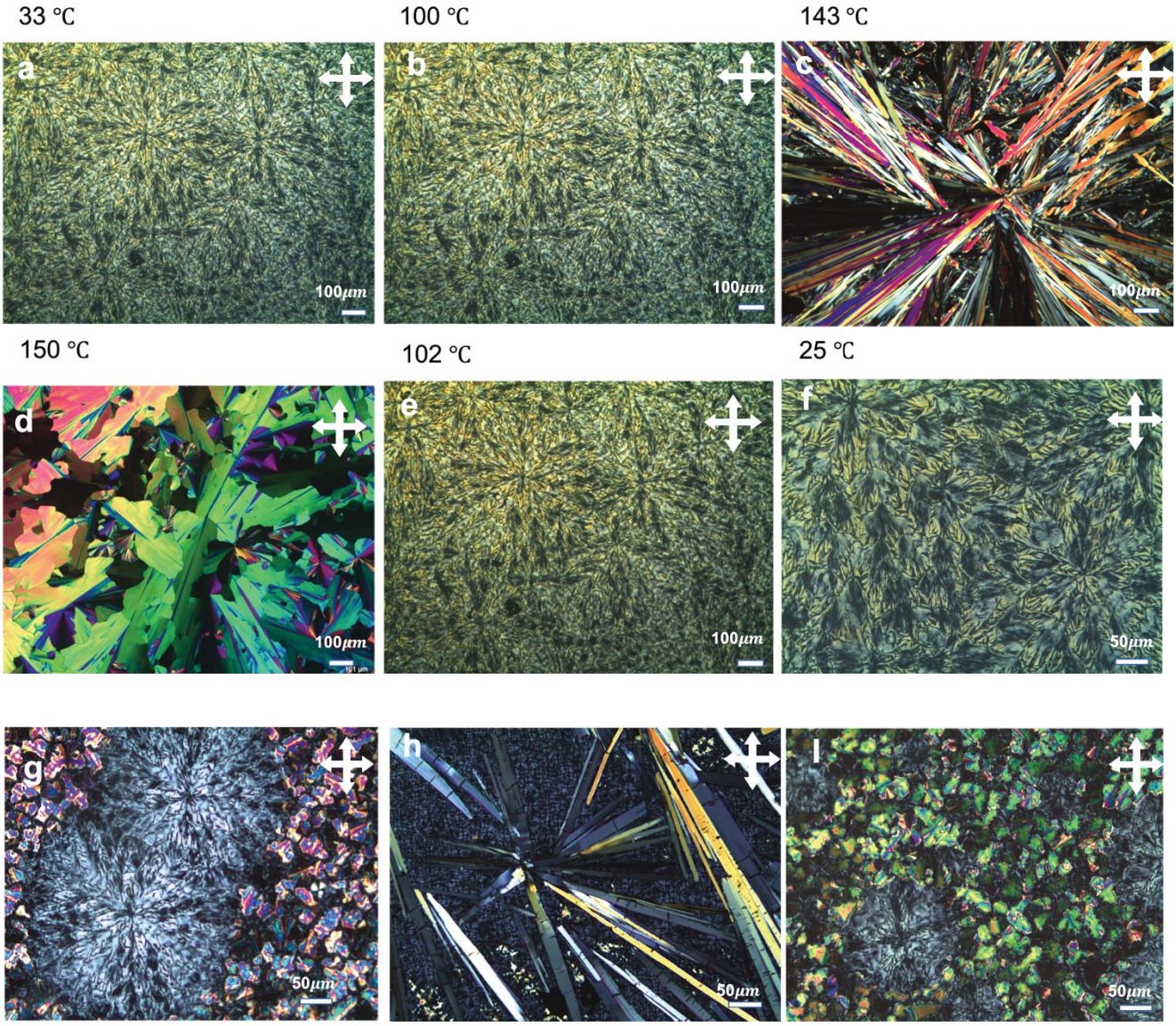


**Figure S14:** POM images (crossed polarizers) of *p*-(*R*)-**4**: **a** – **c** on heating by rate 5 °C min$^{-1}$. **a** and **b** show the B4 phase at 33 °C and 100 °C; image **c** was taken at 143 °C showing the texture of the $Col_{ob}$ phase. It clears to the isotropic liquid phase at 156 °C **d** – **f** on cooling at the same rate. **d** shows the $Col_r$ at 150 °C; this is the phase observed on cooling from the isotropic liquid phase. **e** and **f** show the B4 phase at 102 °C and 25 °C. It transitions to the $Col_r$ at 152 °C and to the B4 phase (HLNC morphology) at 141 °C. Both Col phases exist in a narrow temperature range. **g** – **I** on fast cooling (quench) of the material from isotropic liquid phase (different parts of the sample). It turns out there two phases $Col_r$ and B4 at room temperature. In another words, there is coexistence of these two phases. The material was sandwiched between two clean, untreated glass substrates (gap: 50 μm).

**5.2** POM images for material *p*-(S)-**4** on heating and cooling by rate 5 °C min$^{-1}$ as well as on fast cooling.

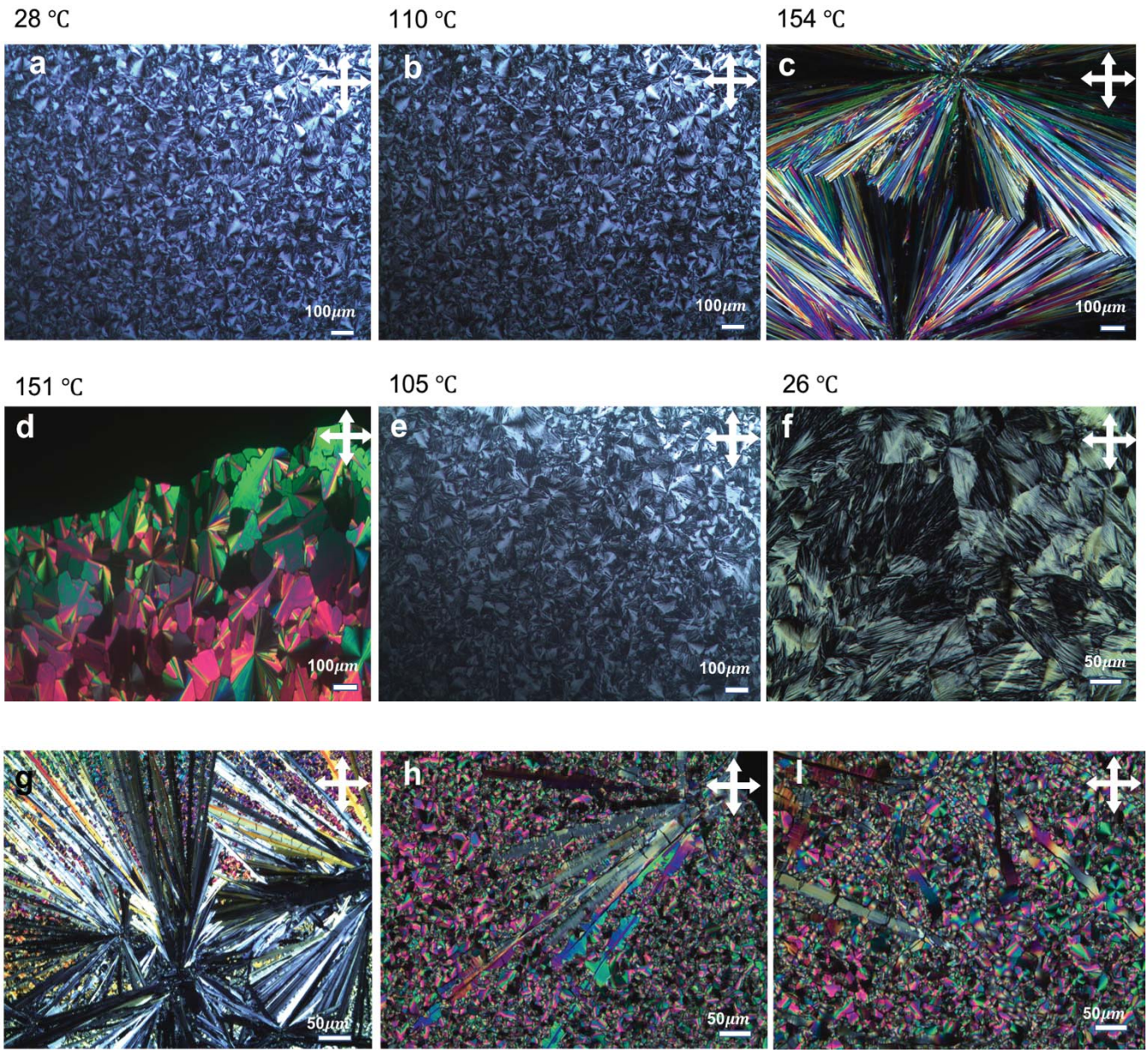


**Figure S15:** POM images (crossed polarizers) for material *p*-(*S*)-**4**: **a** – **c** on heating. **a** and **b** show the texture of the B4 phase, and **c** shows the texture of the $Col_{ob}$ phase, which clears to the isotropic liquid phase at 158 °C. **d** – **f** are on cooling. **d** shows the texture of the $Col_r$ phase at 151 °C. **e** and **f** show the B4 phase with changing birefringence due to a decrease in temperature. **g** – **I** shows photomicrographs taken when the sample was quenched from the isotropic liquid state, which show coexistence of $Col_r$ and B4 phase (HLNC morphology) (taken at room temperature).

## 6. DSC Data

**Table S1.** DSC Data for compounds *p*-(*R*)-**4** and *p*-(*S*)-**4**.

| Treatment of the sample prior to DSC measurements | Compound | Rate[a] / °C min$^{-1}$ | Transition Temperature [Enthalpy] on heating / °C [kJ mol$^{-1}$] | Transition Temperature [Enthalpy] on cooling[b] / °C [kJ mol$^{-1}$] |
|---|---|---|---|---|
| Heated to isotropic phase and cooled back to room temperature | *p*-(*R*)-**4** | 5 | 151.6 [32.5]; 157.0 [4.3] | 145.1 [−10.9]; 140.5 [−33.8] |
| | *p*-(*S*)-**4** | 5 | 152.4 [33.8]; 157.9 [39.8] | 150.2 [−34.1]; 141.8 [−28.8] |
| Fast heating to isotropic phase and fast cooling to room temperature | *p*-(*R*)-**4** | 50 | 153.4 [47.3] | 142.6 [−13.5]; 134.4 [−31.2] |
| | *p*-(*S*)-**4** | 50 | 155.0 [47.9] | 147.6 [−18.6]; 132.8 [−25.6] |

[a] Heating/cooling rate for the DSC experiment, [b] peak values are used.

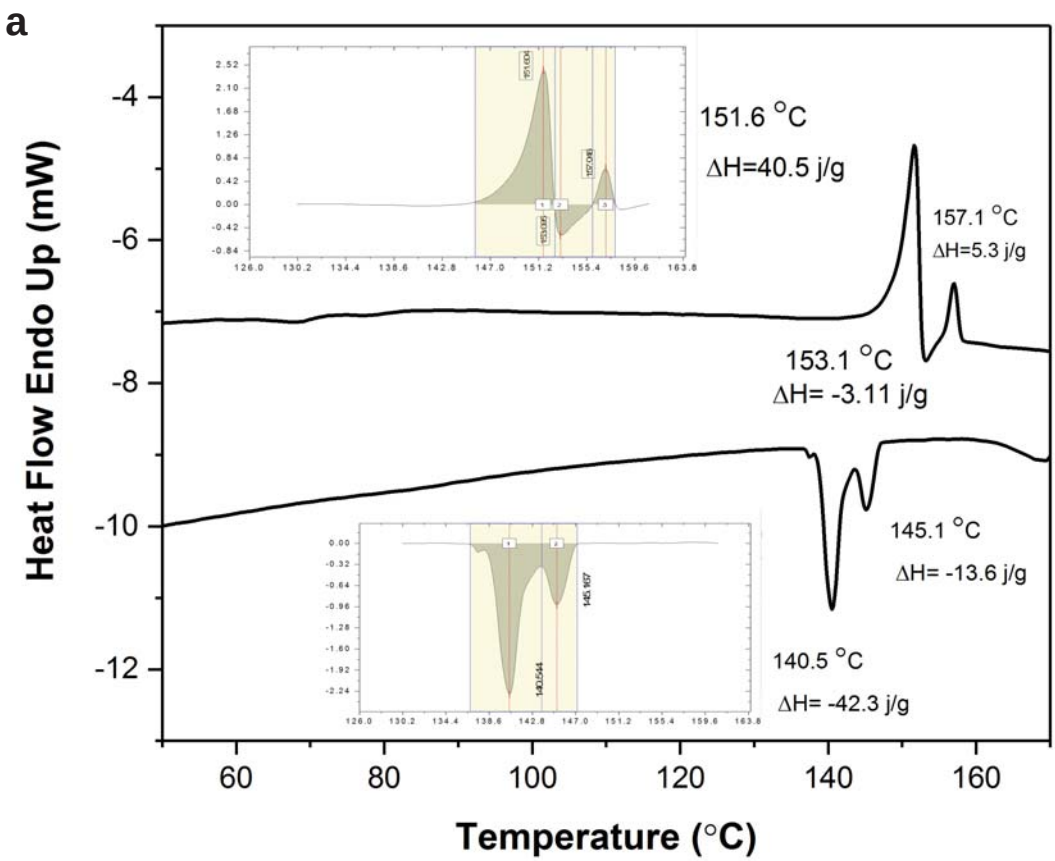

**b**

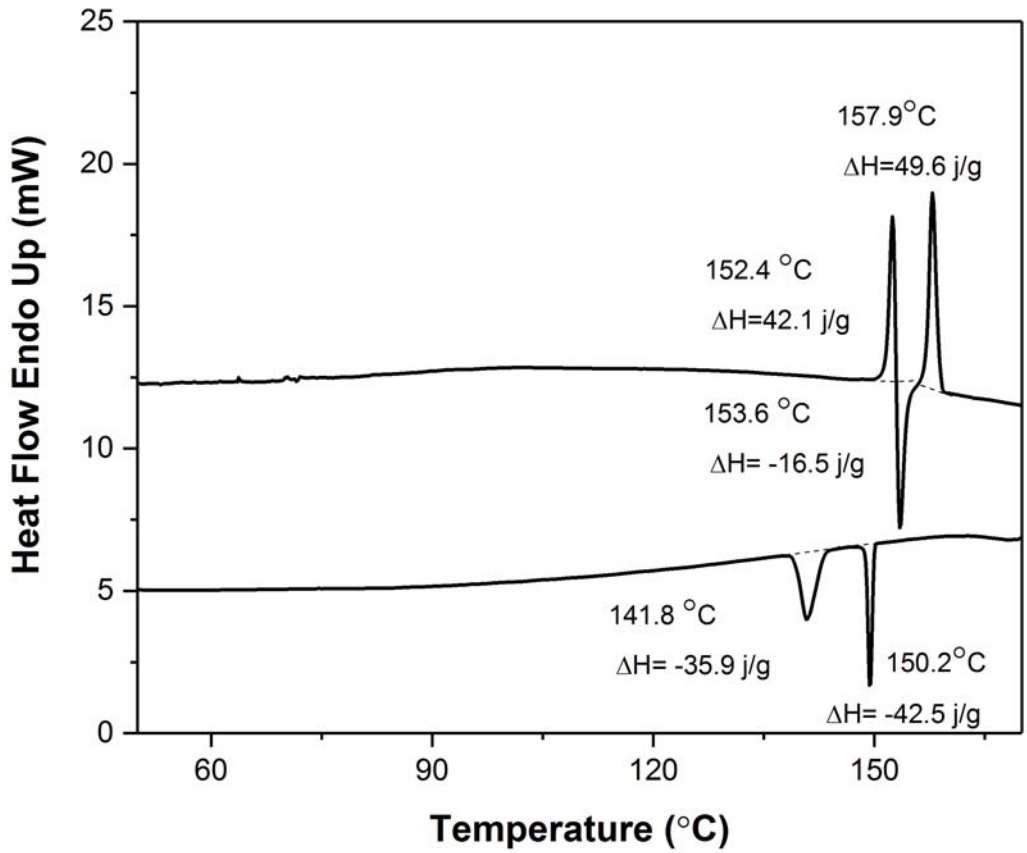
Heat Flow Endo Up (mW)
Temperature (°C)
157.9°C
ΔH=49.6 j/g
152.4 °C
ΔH=42.1 j/g
153.6 °C
ΔH= -16.5 j/g
141.8 °C
ΔH= -35.9 j/g
150.2°C
ΔH= -42.5 j/g

**c**

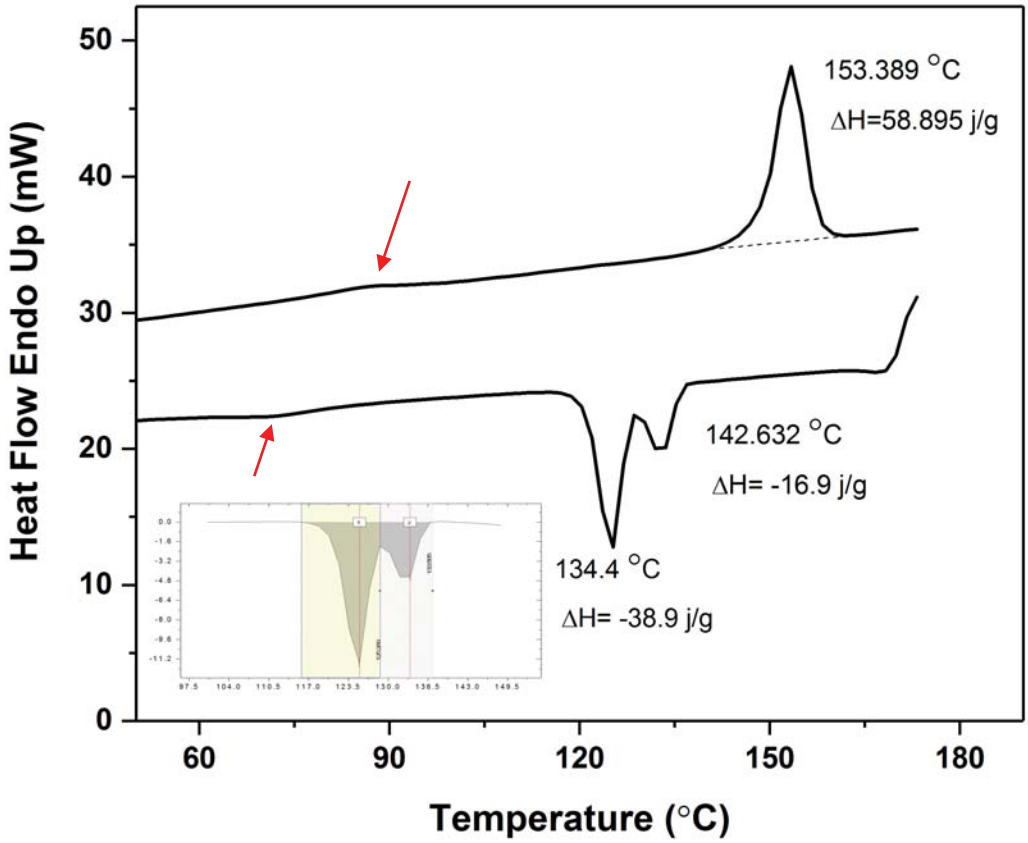
Heat Flow Endo Up (mW)
Temperature (°C)
153.389 °C
ΔH=58.895 j/g
142.632 °C
ΔH= -16.9 j/g
134.4 °C
ΔH= -38.9 j/g

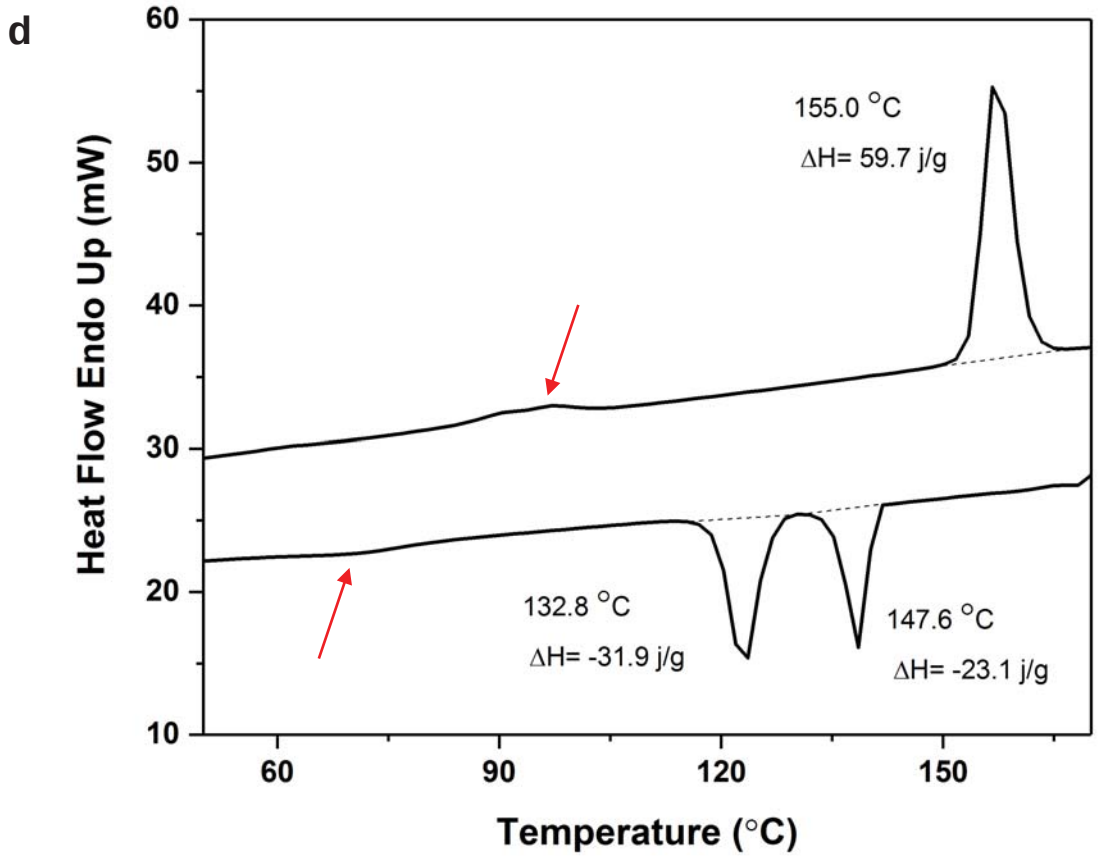


**Figure S16**: DSC plots: **a** and **b** are the DSC plots for *p*-(*R*)-**4** and *p*-(*S*)-**4**, heated to the isotropic liquid phase and then cooled back to room temperature at a rate of 5 °C min$^{-1}$. On heating (upper curves), each sample forms the B4 phase (HLNC morphology) and the B1 ($Col_{ob}$) phase based on X-ray and POM observations. On cooling (lower curves), each compound forms the B1 ($Col_r$) and the B4 phase (HLNC morphology). Deconvolution and baseline-correction are shown in the two insets in **a**. **c** and **d** show the plots related to *p*-(*R*)-**4** and *p*-(*S*)-**4**, accordingly, the same samples when the rate of heating and cooling was increased 10-fold (50 °C min$^{-1}$). On heating, the B1 phase has not been observed and the samples go directly to the isotropic liquid phase. Inset in **c** shows deconvolution and baseline-correction. On cooling, the phase sequence appears identical to the sequence observed at the slower cooling rate, although the transition temperatures are shifted to significant lower temperature values and are much broader. The phase coexistence seen by POM could not be followed by DSC since the thermal quench can instrumentally not be reproduced. Typical for B4 phases after thermal treatment, the DSC traces at the faster heating/cooling rate show broad shoulders indicating a phase transition to the B4 phase (indicated by red arrows).[5]

## 7. Solution CD spectra

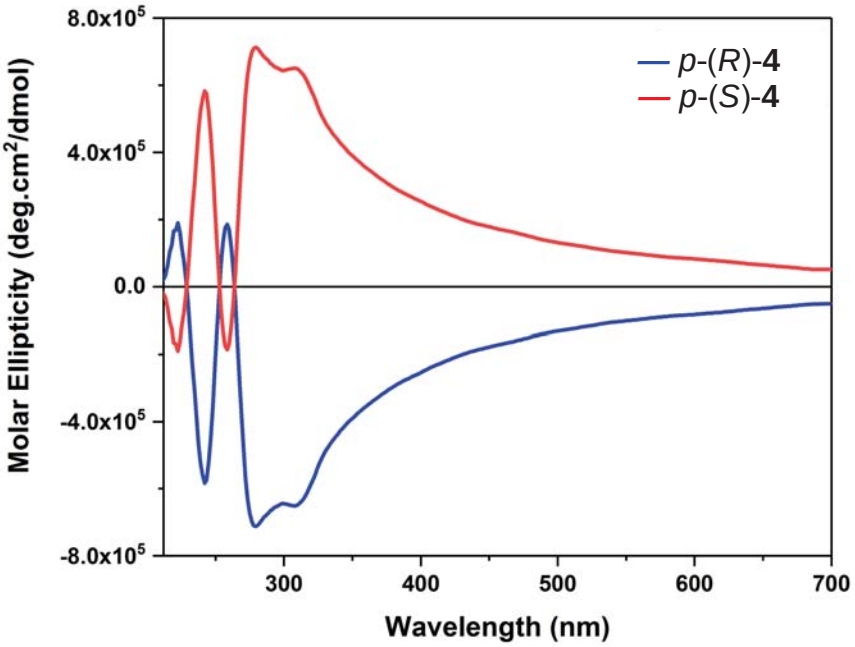


**Figure S17**: Solution CD spectra for *p*-(*R*)-**4** and *p*-(*S*)-**4** at a concentration of 0.18 mM in *n*-hexane. These spectra show characteristic bands for the individual chiral molecules in the UV wavelength spectral range in solution and a shoulder starting at around 320 nm that falls or rises to almost zero through the visible spectral range. As shown by Hsu and co-workers,[6, 7] bent core molecules similar to *p*-(*R*)-**4** and *p*-(*S*)-**4** are capable of forming helical ribbons or tubular structures in gels formed by these molecules in organic solvents. As shown in Figure S24, also *p*-(*R*)-**4** and *p*-(*S*)-**4** form structures in such gels in *n*-hexane upon standing that not captured by these solution CD spectra.

## 8. Synchrotron SAXD data and indexing for XRD data

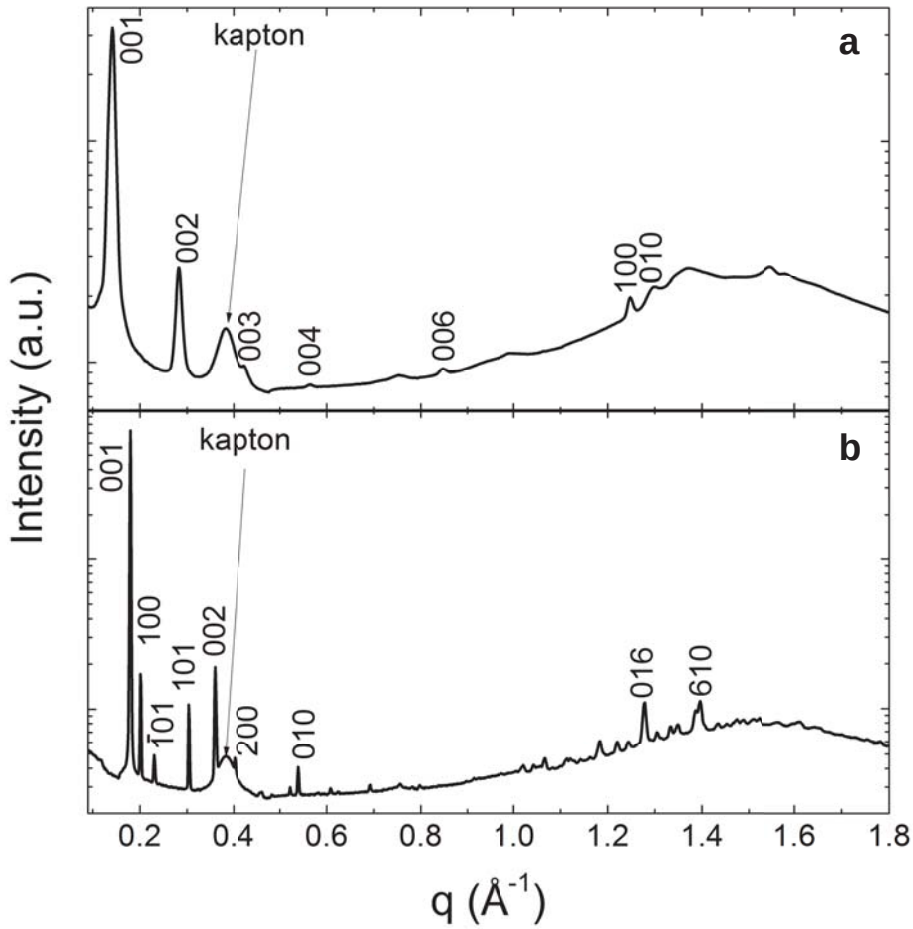


**Figure S18**: Small angle X-ray scattering data for: **a** the B4 phase (HLNC morphology) obtained after slow cooling from the isotropic liquid phase at room temperature and **b** the $Col_{ob}$ phase obtained on slow heating (5 °C min$^{-1}$) at 155 °C.

**Table S2**: Indexing and measured scattering vectors *q* for XRD data from Fig. 3 and Fig. S18. Further detailed information about the XRD data (*e.g.* experimental reflection intensities, calculated *q* values, and refined lattice parameter values) is available upon request from the authors.

| **$Col_{ob}$ – *P*2** | |
|---|---|
| hkl | *q* ($Å^{-1}$) |
| 001 | 0.17771 |
| 100 | 0.20039 |
| $10\bar{1}$ | 0.23051 |
| 101 | 0.3001 |
| 002 | 0.35444 |
| $10\bar{2}$ | 0.35953 |
| 200 | 0.40057 |
| 010 | 0.68997 |
| 111 | 0.75278 |
| 210 | 0.79802 |
| 310 | 0.91533 |
| 213 | 1.01462 |
| $50\bar{4}$ | 1.06676 |
| $21\bar{5}$ | 1.11303 |
| 502 | 1.1449 |
| $60\bar{3}$ | 1.18143 |
| $51\bar{3}$ | 1.2191 |
| $21\bar{6}$ | 1.24395 |
| $31\bar{6}$ | 1.27927 |
| 107 | 1.30681 |
| 306 | 1.34908 |
| 610 | 1.38551 |
| $70\bar{4}$ | 1.39713 |
| $12\bar{3}$ | 1.47418 |
| $70\bar{6}$ | 1.52447 |
| | |

| **B4** | |
|---|---|
| hkl | *q* ($Å^{-1}$) |
| 001 | 0.14102 |
| 002 | 0.28202 |
| 003 | 0.4222 |
| 004 | 0.56299 |
| 005 | 0.70361 |
| 006 | 0.84402 |
| 007 | 0.98491 |
| 101 | 1.2519 |
| 103 | 1.31389 |
| 104 | 1.36561 |
| 013 | 1.39399 |
| 0011 | 1.54653 |
| | |

| **$Col_r$ – *c2mm*** | |
|---|---|
| hkl | *q* ($Å^{-1}$) |
| 101 | 0.20884 |
| 002 | 0.30732 |
| 301 | 0.45026 |

## 9. Additional SEM, TEM and AFM images

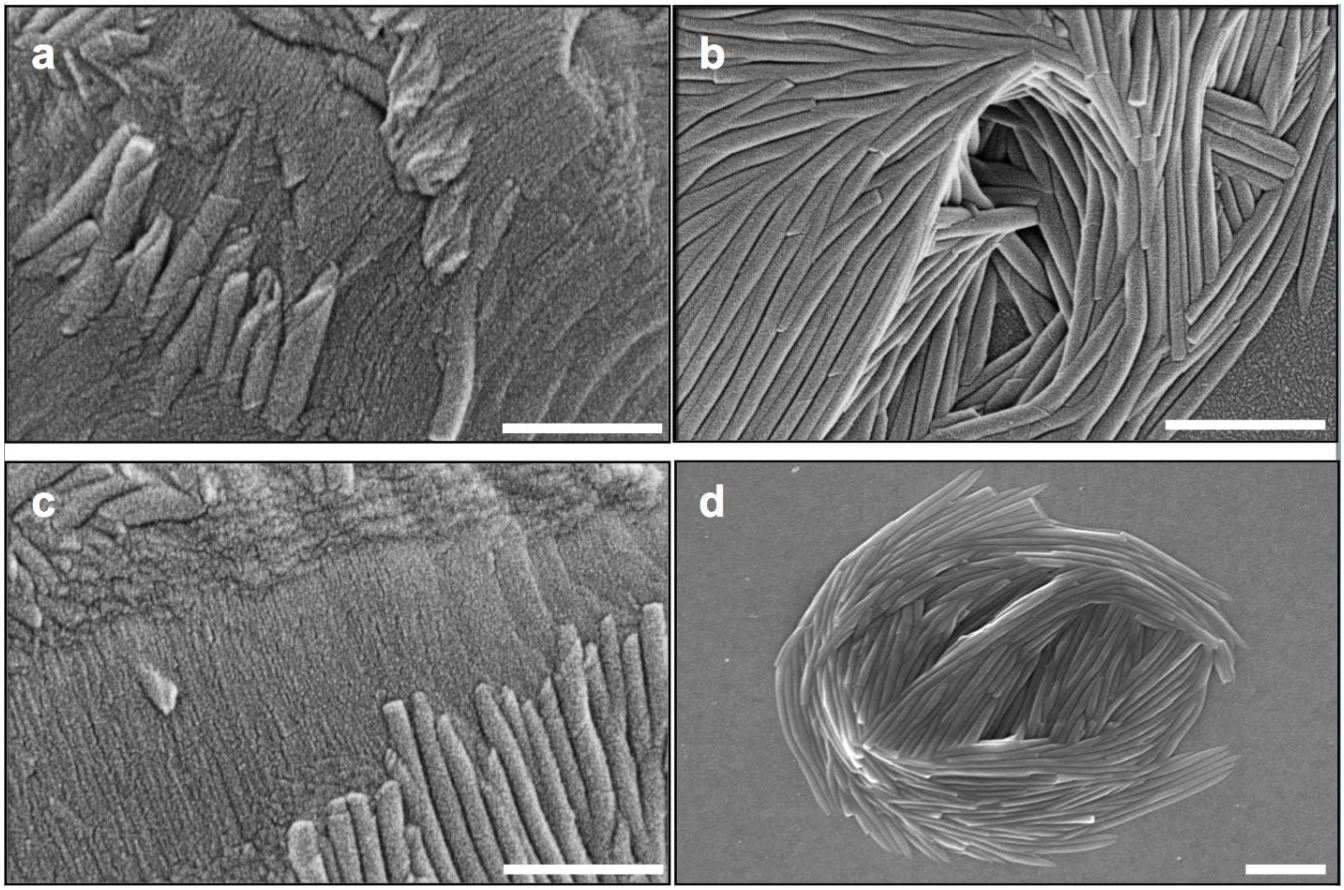


**Figure S19**: SEM images of *p*-(*R*)-**4** and *p*-(*S*)-**4** obtained after treating the samples at different cooling rates: **a** *p*-(*R*)-**4** after rapid cooling to room temperature from the isotropic liquid phase showing the biphasic nature of the HLNC and another phase (most likely $Col_r$ phase based on X-ray and POM studies). Short twisted HLNCs, arranged side-by-side are separated by relatively smooth, featureless areas. **b** *p*-(*R*)-**4** after slow cooling at a rate of 5 °C $min^{-1}$; the splitting/merging of the nanocylinders is clearly visible. **c** *p*-(*S*)-**4** after rapid cooling showing phase co-existence. Again, short twisted HLNCs, arranged side-by-side are separated by relatively smooth, featureless areas. **d** *p*-(*S*)-**4** after slow cooling showing the formation of a 'nest-like' structure. A 20-nm layer of Pd metal was coated onto these samples for SEM images. The scale bars are 500 nm.

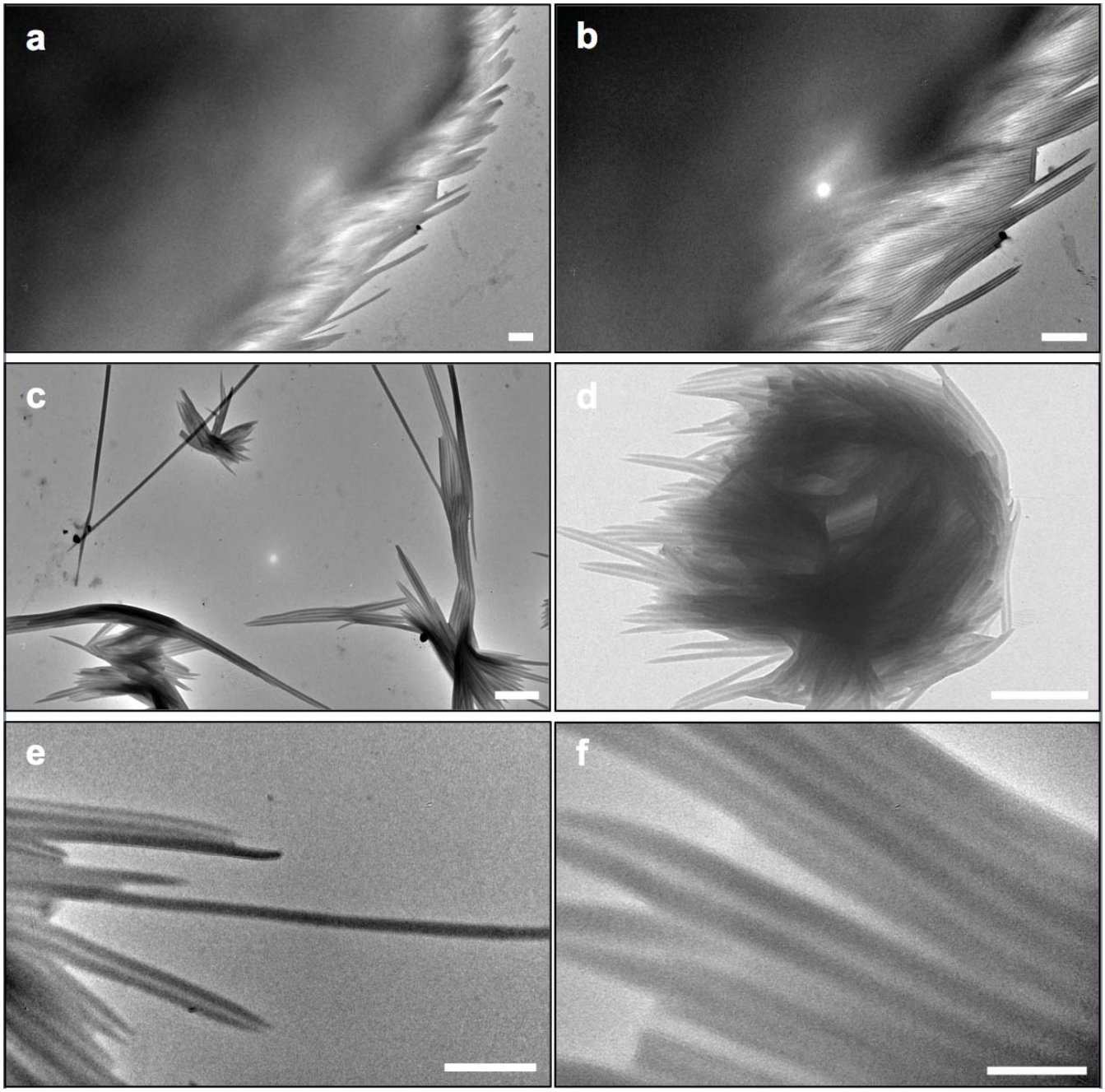


**Figure S20**: TEM images of *p*-(*R*)-**4** and *p*-(*S*)-**4** obtained after treating the samples at different cooling rates: **a**, **b** *p*-(*S*)-**4** after rapid cooling to room temperature from the isotropic liquid phase (scale bars are 1 µm). HLNCs appear to grow out of a smooth, featureless bulk – consistent with the biphasic nature of the material after thermal quenching. **c**, **d** *p*-(*R*)-**4** after slow cooling at a rate of 5 °C $min^{-1}$. Solid HLNCs form various shapes including the nest-like structures already observed by SEM (image **d**) – scale bars are 1 µm. **e**, **f** Zoomed in TEM images show the solid nature of the HLNCs – no gradient of electron density supports the assumption that these HLNCs are not hollow cylinders or tubes, but solid structures (scale bars: **e**, 500 nm; **d**, 200 nm).

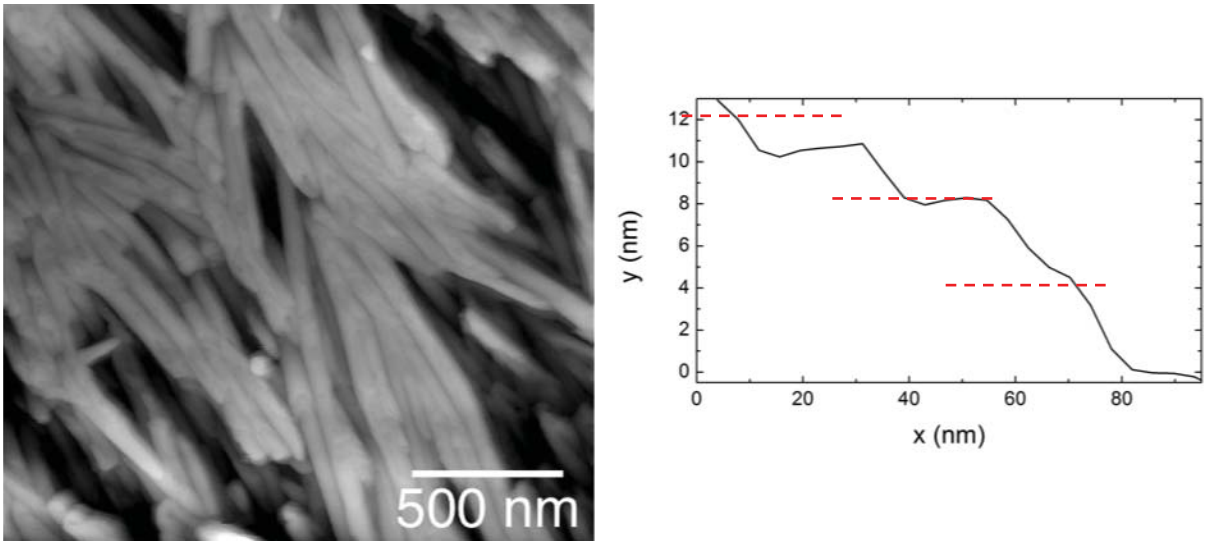


**Figure S21**: AFM height image of *p*-(*S*)-**4** reveals peeled multi-wall nanocylinders. The thickness of the nanocylinders is around 80 nm. The cross-section of the peeled nanocylinders shown in the *x*-*y* plot (*y* is the height) shows a layer thickness of 4 nm (the step at *y* ~ 10 nm could have been caused by a lower lying nanocylinders).

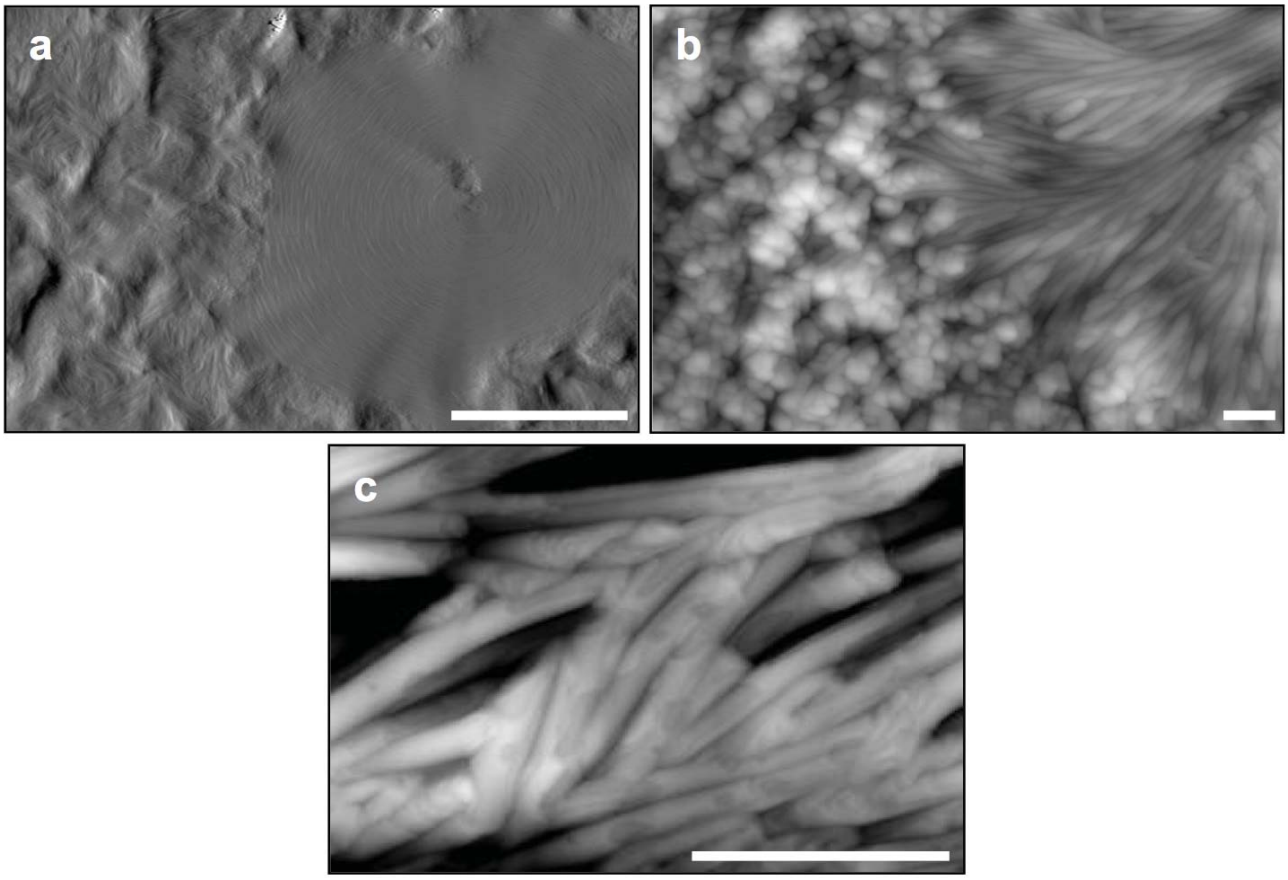


**Figure S22**: **a** AFM image of *p*-(*R*)-**4** after rapid cooling, confirming again the biphasic nature (scale bar: 20 µm). **b** AFM image of *p*-(*S*)-**4** after rapid cooling, also confirming the biphasic nature (scale bar: 200 nm). **c** Height image of *p*-(*R*)-**4** showing the peeled HLNCs with 80 nm width and 4 nm layers (scale bar 1 µm).

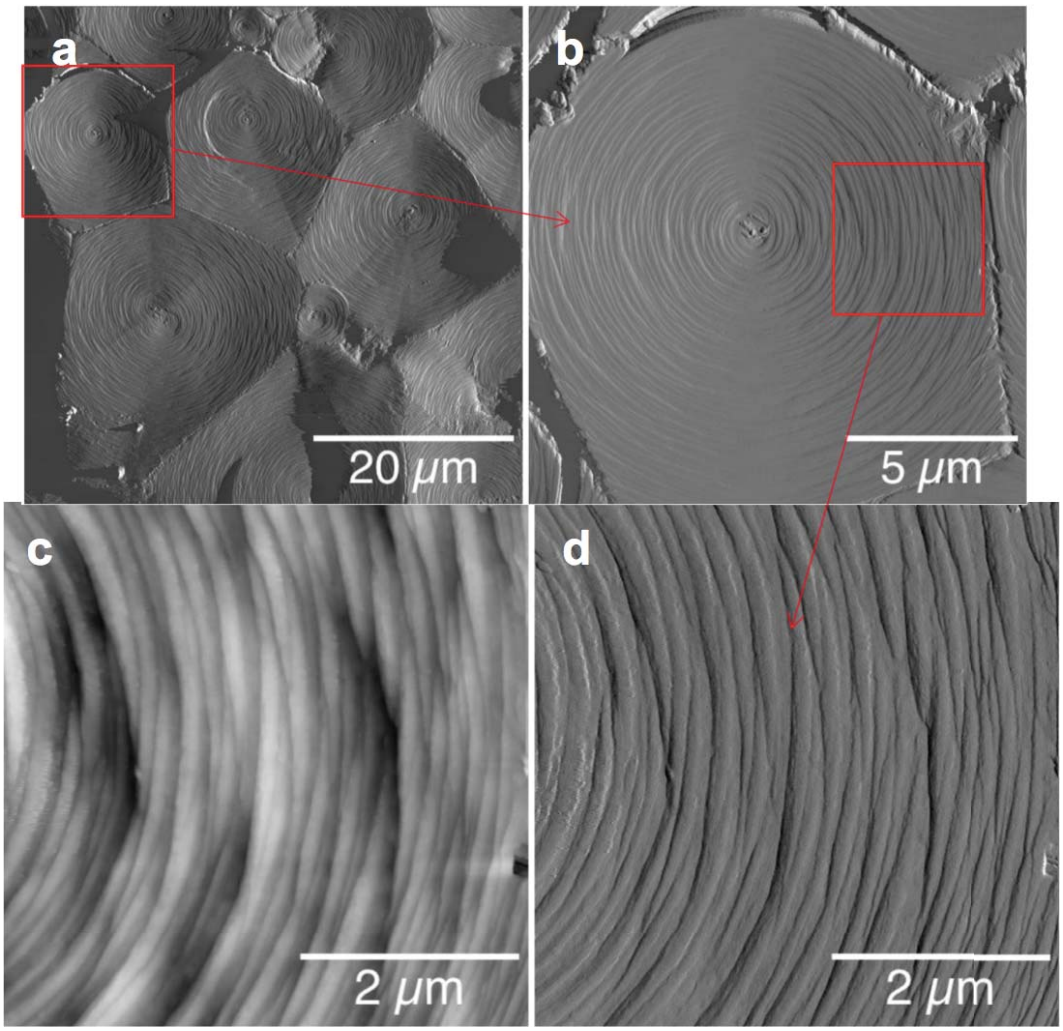


**Figure S23**: AFM images of *p*-(*S*)-**4** after fast cooling: **a**, **b** amplitude images, **c** zoomed in height and **d** amplitude image. In this particular case, the sample was rapidly cooled but not covered by glass (free surface – contact to air). As for the B7 filaments, the free surface appears to favor the formation of the coaxial HLNC structures.

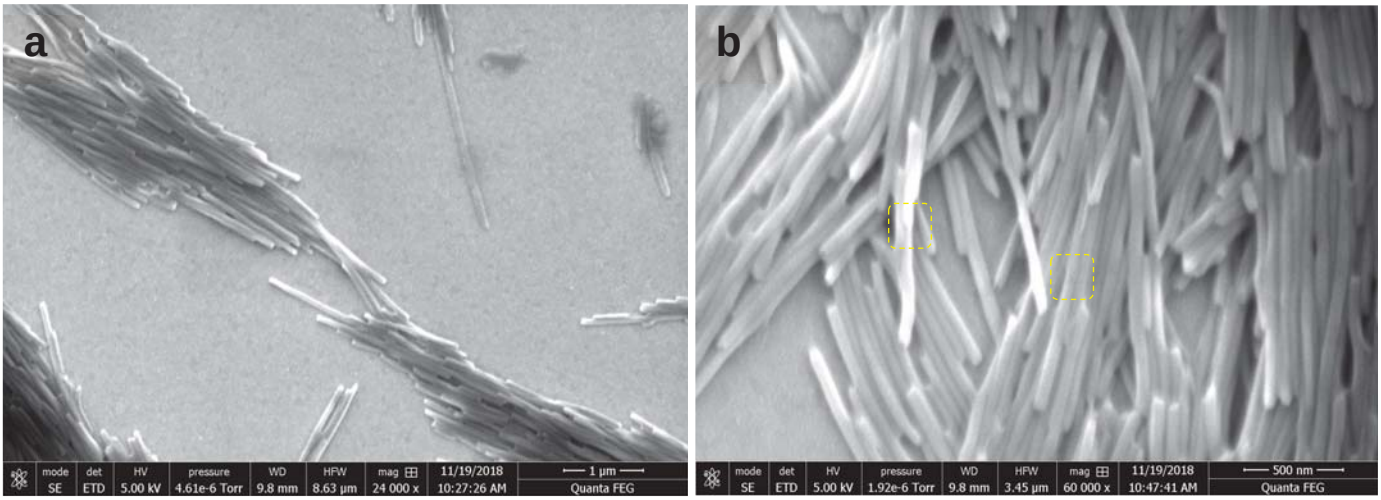


**Figure S24**: **a**, **b** SEM images of rod-like structures formed by *p*-(*R*)-**4** formed in *n*-hexane gels upon standing. See comment in caption to Figure S17. The size and dimensions of these nanocylinders matches those found for the condensed phase HLNCs forming the B4 phase (diameter about 80 nm). They do not appear to be hollow tubular structures but rather solid structures that we suggest follow the heliconical layering described for the bulk B4 HLNC super-structures. However, many of them appear shorter in length (on average 1 – 2 µm) and a heliconical twist is only rarely visible (see yellow highlighted areas), but matches the twist sense found for the condensed phase HLNC morphology.

## 10. Transmission and Reflection UV-vis spectra

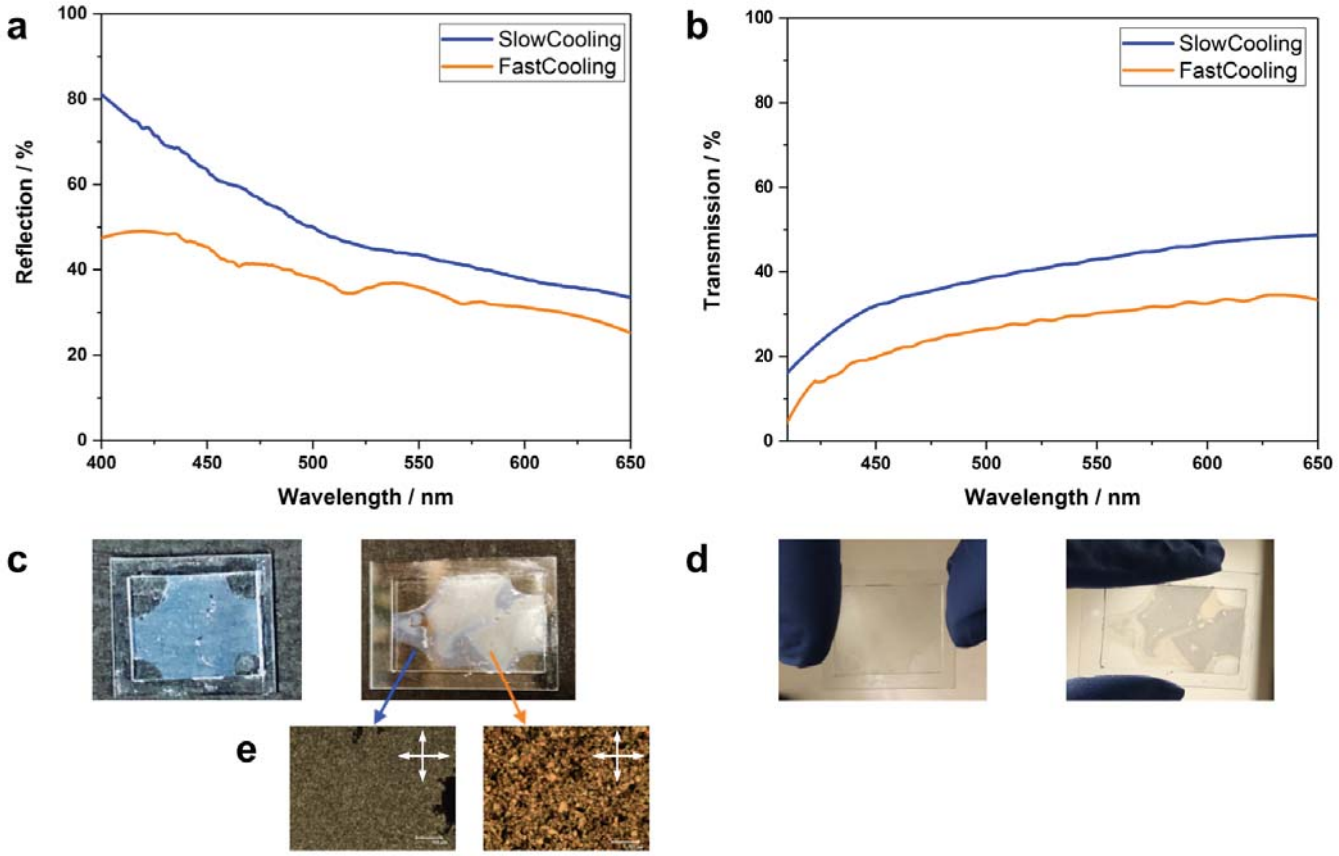


**Figure S25**: **a** UV-vis reflection and **b** UV-vis transmission spectra of the slow and fast cooled sample of *p*-(*S*)-**4**, respectively (blue curves: slow cooled; orange curves: fast cooled). **c**, **d** Sample photographs in reflection and transmission. Note, the sample appears blue only in reflection after slow cooling (in the B4 phase with HLNC morphology) and only in the regions showing the texture of the B4 phase of the biphasic sample after rapid cooling. The textures observed by POM between crossed polarizers (indicated by the white arrows) in each of these two regions are shown in **e**.

## 11. Computational methods

All the atomistic calculations were performed using the GROMACS 4.6.7[8] package with a modified GAFF force field (GAFF-LCFF) developed earlier.[9,10] The energy function employed in the calculations is given by the equation:

$$\begin{aligned} E^{\mathrm{MM}} &= \sum_{\text{bonds}} K_{\mathrm{r}}(r - r_{\mathrm{eq}})^2 + \sum_{\text{angles}} K_{\theta}(\theta - \theta_{\mathrm{eq}})^2 \\ &+ \sum_{n=0}^{5} C_n(\cos(\psi)^n + \sum_{\text{impropers}} K_{\mathrm{d}}(1 + \cos(n_{\mathrm{d}}\omega - \omega_{\mathrm{d}}) \\ &+ \sum_{i>j}^{N} \left[ 4\epsilon_{ij} \left( \left(\frac{\sigma_{ij}}{r_{ij}}\right)^{12} - \left(\frac{\sigma_{ij}}{r_{ij}}\right)^{6} \right) + \frac{1}{4\pi\varepsilon_0} \frac{q_i q_j}{r_{ij}} \right], \end{aligned} \tag{1}$$

where $r_{eq}$, $\theta_{eq}$ are structural equilibration parameters, $K_r$, $K_\theta$ and $C_n$ are force constants, $\varepsilon_{ij}$ and $\sigma_{ij}$ are the usual Lennard-Jones parameters and $q_i$ and $q_j$ are partial electronic charges. Changes in $E^{MM}$ arising from deviations in improper dihedral angles, $\omega$, are represented by cosine functions using the force constants, $K_d$, the harmonic coefficients, $n_d$ and the phase angles, $\omega_d$. Throughout this work these improper dihedral angle parameters have been applied unchanged from the original GAFF force field. The standard Lorentz-Berthelot mixing rules of $\varepsilon_{ij} = (\varepsilon_i \varepsilon_j)^{1/2}$ and $\sigma_i = (\sigma_i + \sigma_j)/2$ have been applied for calculating the LJ parameters between different types of atoms. All molecules selected for these studies were built using the AVOGADRO 1.0.0 program. The OpenBabel code was used to extract coordinate files including the connectivity information. The Antechamber software from AmberTools 1.4 was used to generate GAFF topologies, with the point charges derived through the AMI-BCC method. The GAFF topologies and coordinate files were converted into the GROMACS format using the acpype_py script.[11] Single molecule stochastic dynamics (SD) atomistic simulations were performed for each mesogen in the gas phase, at 300 K and for a total of 500 ns. The geometry of each mesogen was optimized in vacuum using DFT methods and the B3LYP hybrid atfunctional, combined with the 6-311G(d,p) basis set.

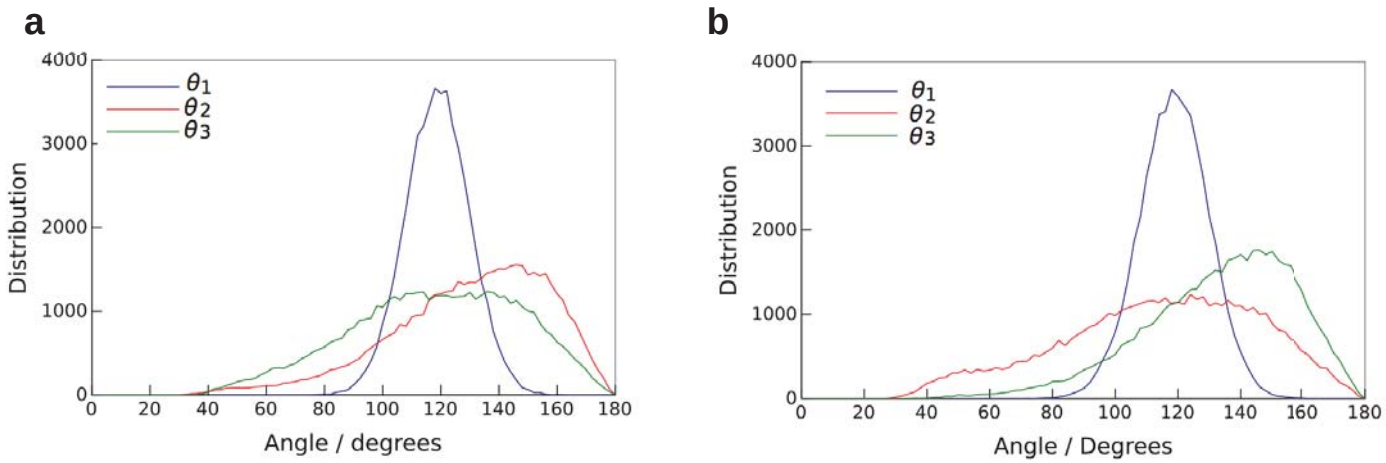


**Figure S26**: Angle distribution functions (arbitrary units) for the aromatic core and core-chain angles for: **a** *m*-(*R*)-**3** and **b** *p*-(*R*)-**4**.

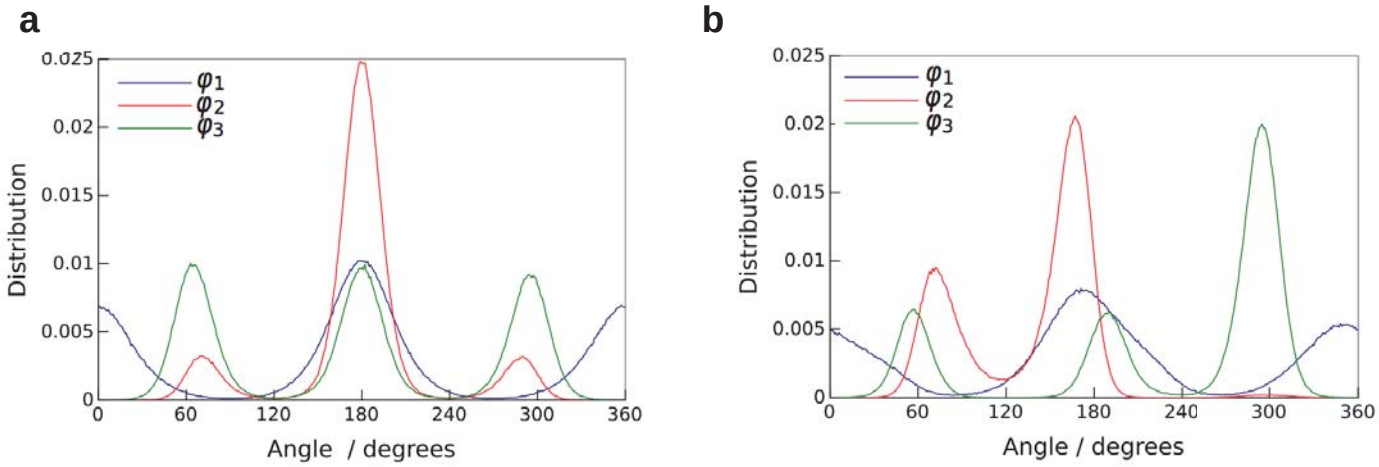


**Figure S27**: Dihedral distribution functions for selected dihedrals for the *para*-side of: **a** *m*-(*R*)-**3** and **b** *p*-(*R*)-**4**.

An indication of the molecular dimensions, and hence overall shape, can be obtained from the average moment of inertia tensor, $\langle I \rangle$ where $\langle I_1 \rangle$, $\langle I_2 \rangle$ and $\langle I_3 \rangle$ are the averaged principle moments of inertia. These values enable the average length, $\langle L \rangle$, breadth, $\langle B \rangle$ and width, $\langle W \rangle$ of a mesogen to be calculated using $a = \sqrt{2.5(I_2 + I_3 - I_1)m}$ and cyclic permutations for $b$ and $c$.[12] Average aspect ratios $(L/B)$ can also be obtained where in this instance $B$ represents $(breadth + width)$ / 2. Table S3 shows subtle differences in average molecular dimensions between the two mesogens. A small reduction in average length, coupled with a small increase in average width and breadth, is observed for *p*-(*R*)-**4**, leading to a minor reduction in the length to breadth ratio, compared with *m*-(*R*)-**3**. This may reflect a subtle change in the conformational distributions between the two mesogens.

**Table S3:** Average molecular dimensions for *m*-(*R*)-**3** and *p*-(*R*)-**4** obtained from single molecule stochastic dynamics calculations.

| | $\langle L \rangle$ / Å | $\langle B \rangle$ / Å | $\langle W \rangle$ / Å | $\langle L/B \rangle$ |
|---|---|---|---|---|
| *m*-(*R*)-**3** | 47.91 | 15.15 | 5.70 | 4.60 |
| *p*-(*R*)-**4** | 47.66 | 15.20 | 5.80 | 4.54 |

Bulk phase simulations of the bent-core mesogens were performed on 256 molecules. A cut-off of 1.2 nm was used for short-range non-bonded interactions, the Particle Mesh Ewald (PME) method was used for long-range electrostatics, and the simulations employed the usual corrections for the pressure and potential energies to compensate for the truncation of the van der Waals interactions. The Berendsen thermostat and barostat was used for initial simulation setups compressing, at 100 bar pressure, from low-density random arrangements of molecules, followed by equilibration and production runs with a Nosé–Hoover thermostat, and Parrinello–Rahman barostat once liquid state densities were reached. Isotropic pressure coupling and a compressibility of 4.6 105 bar1 was used throughout. Bond lengths were kept fixed at their equilibrium values using the LINCS algorithm and a timestep of 2 fs was employed. Each system was progressively cooled at 10 K intervals for a total simulation time of 360 ns at each temperature point.

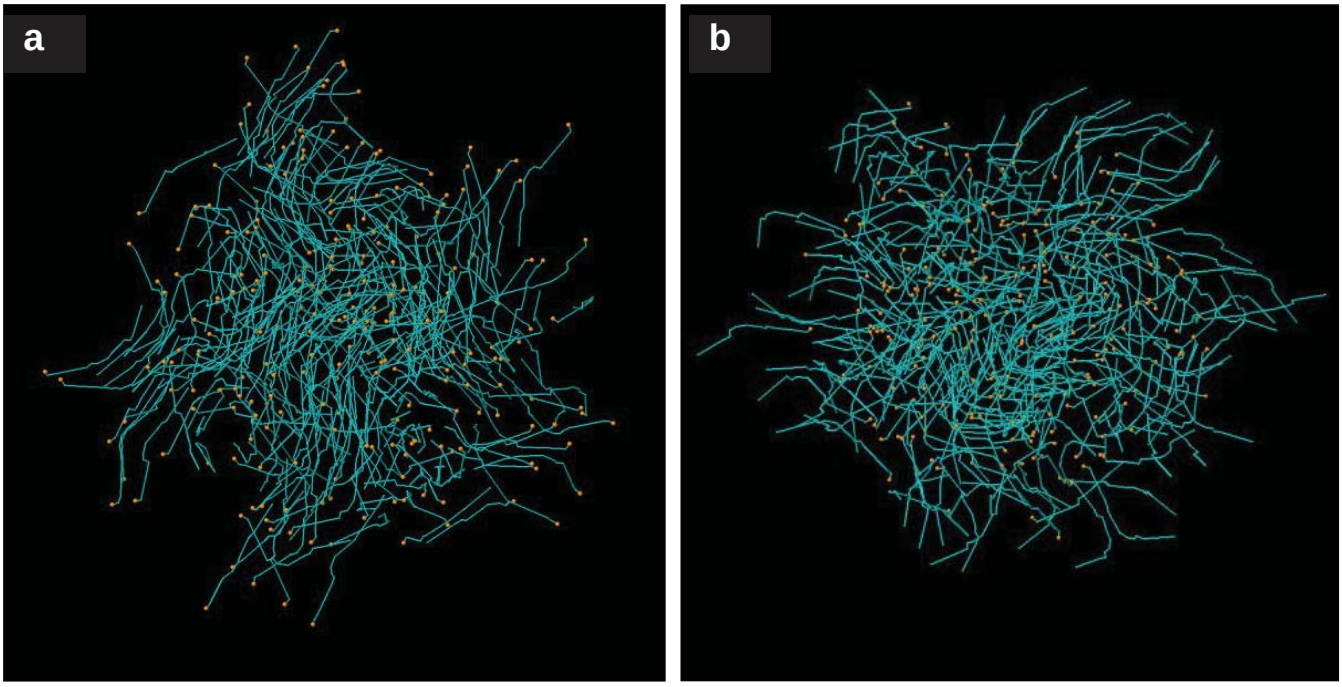


**Figure S28**: Enlarged images (from Fig. 7 in the article): Simplified representations of snapshots from the molecular dynamics simulations (*N* = 256 molecules) of: **a** *m*-(*R*)-**3** at *T* = 350 K and **b** *p*-(*R*)-**4** at *T* = 380 K. Chiral centers highlighted in orange.

**References**


1. A. Hexemer, W. Bras, J. Glossinger, E. Schaible, E. Gann, R. Kirian, A. MacDowell, M. Church, B. Rude and H. Padmore, *J. Phys. Conf. Ser., XIV International Conference on Small-Angle Scattering (SAS09), 2010,* ***247****, 012007.*
2. J. Ilavsky, *J Appl Crystallogr*, 2012, **45**, 324-328.
3. L. Li, M. Salamończyk, S. Shadpour, C. H. Zhu, A. Jákli and T. Hegmann, *Nat. Commun.*, 2018, **9**, 714.
4. L. Li, M. Salamończyk, A. Jákli and T. Hegmann, *Small*, 2016, **12**, 3944-3955.
5. E. Tsai, J. M. Richardson, E. Korblova, M. Nakata, D. Chen, Y. Q. Shen, R. F. Shao, N. A. Clark and D. M. Walba, *Angew. Chem. Int. Edit.*, 2013, **52**, 5254-5257.
6. S. C. Lin, T. F. Lin, R. M. Ho, C. Y. Chang and C. S. Hsu, *Adv. Funct. Mater.*, 2008, **18**, 3386-3394.
7. S. C. Lin, R. M. Ho, C. Y. Chang and C. S. Hsu, *Chem.-Eur. J.*, 2012, **18**, 9091-9098.
8. S. Pronk, S. Pall, R. Schulz, P. Larsson, P. Bjelkmar, R. Apostolov, M. R. Shirts, J. C. Smith, P. M. Kasson, D. van der Spoel, B. Hess and E. Lindahl, *Bioinformatics*, 2013, **29**, 845-854.
9. N. J. Boyd and M. R. Wilson, *Phys. Chem. Chem. Phys.*, 2015, **17**, 24851-24865.
10. N. J. Boyd and M. R. Wilson, *Phys. Chem. Chem. Phys.*, 2018, **20**, 1485-1496.
11. A. W. Sousa da Silva and W. F. Vranken, *BMC Research Notes*, 2012, **5**, 367.
12. M. R. Wilson and M. P. Allen, *Liq. Cryst.*, 1992, **12**, 157-176.